Università degli Studi di Trieste

XXXV Ciclo del Dottorato di Ricerca in
Earth Science, Fluid-Dynamics, and Mathematics.
Interactions and Methods

PO FRIULI VENEZIA GIULIA - FONDO SOCIALE EUROPEO
2014/2020

CAVITATION MODELS FOR SHIP PROPELLERS

Settore scientifico-disciplinare: ICAR/01

Ph.D. Student:	Andrea Savio
Ph.D. Program Coordinator:	Prof. Stefano Maset
Supervisor:	Prof. Vincenzo Armenio
Co-Supervisor:	Prof. Marta Cianferra
Co-Supervisor:	Prof. Rickard Bensow

Academic Year 2021–2022

Author: Andrea Savio

e-mail: andrea.savio@phd.units.it

Affiliation: Doctoral School in
"Earth Science, Fluid-Dynamics, and Mathematics.
Interactions and Methods".
Dipartimento di Ingegneria e Architettura,
University of Trieste, Piazzale Europa 1,
I-34127 Trieste, Italy

Supervisor: Prof. Vincenzo Armenio

e-mail: vincenzo.armenio@dia.units.it

Affiliation: Dipartimento di Ingegneria e Architettura,
University of Trieste, Piazzale Europa 1,
I-34127 Trieste, Italy

Co-Supervisor: Prof. Marta Cianferra

e-mail: marta.cianferra@dia.units.it

Affiliation: Dipartimento di Ingegneria e Architettura,
University of Trieste, Piazzale Europa 1,

Co-Supervisor: Prof. Rickard Bensow

e-mail: rickard.bensow@chalmers.se

Affiliation: Mechanics and Maritime Sciences,
Division of Marine Technology
Chalmers University of Technology,
se-412 96 gothenburg, sweden,

Day of the defence: 28.09.2023

To cite this work: Andrea Savio, *Cavitation models for ship propellers.*, Ph.D. Thesis, School of Earth Science, Fluid-Dynamics, and Mathematics. Interactions and Methods (2023). Digital resource deposited in the National Legal Deposit service. NBN: *to be assigned*.

Abstract

The research activity reported in this thesis concerns the numerical study of cavitating flows. Academic benchmark cases have been considered to analyze the effectiveness of existing cavitation models.
Cavitation is a phenomenon that has to be avoided because it is the cause of many negative effects, among them, vibrations, local damage to the structure can lead to total structural breakage and are a very important source of noise. An analysis of the Rayleigh-Plesset equation and the stability of the vapor bubble was initially performed analytically and numerically. Having in mind the final application to cases of engineering interest, the best approach in terms of computational cost to model the cavitation is the mixture model, where the processes of condensation and vaporization are treated through the two source terms in a trasport equation for the vapor fraction, one for the condensation process and one for the vaporization one respectively, for which a lot of different models exist in literature.
We compared the results obtained using four different cavitation models, finding some differences among them. Then we propose a normalization method for the evaluation of the empirical multiplying coefficients present in every model by comparing the integral time scale T_{ref} associated with vaporization and condensation processes; the models were compared again with the new normalized coefficients, finding some improvement in the comparison, especially considering the cavitation regime predicted. Since the tip vortex cavitation was found to be the main source of noise in ship propellers, we studied the tip vortex cavitation considering it as an isolated cavitating vortex. We analyzed the vortex forcing different natural modes considering different configurations of the mesh, different values of the empirical coefficients for the cavitation model, and for two-dimensional and three-dimensional cases. The results obtained were in generally good agreement with the analytical solution available in literature [Bosschers (2018)]; the results obtained show that the coefficients are not so important in flow-driven cavitation, if they belong to a correct range, like that which occurs in a vortex; moreover, the geometry and the mesh strongly affect the results, inducing numerical instability and dissipation.

List of Figures

List of Tables

Contents

Chapter 1

Introduzione

In this chapter, we give an overview of the physics of cavitation, its own importance, some literature mathematical methods used for prediction purposes, and the equations used to describe the dynamics of the vapor bubbles.

1.1 cavitation

Every substance in nature may appear in different phgysical states, and, without entering the plasma or other more complicated physics the three main states are, respectively solid, liquid and gas. The state of the substances depends on a number of factors, but mainly on temperature and pressure; in particular, the evaporation process may occur due to an increase of temperature, with the process called boiling, or may be due to a reduction of pressure without a significant change of temperature. This process is called cavitation, as shown in the water phase diagram in Figure 1.1.
Cavitation is a phenomenon that appears usually in high-speed flows when the pressure, due to the energy equilibrium, drops under the vapor tension value threshold leading to change of phase, from liquid to vapor.

Cavitation occurs in several engineering applications, among the others in pipelines, especially near fitting, bottlenecks, or corners where local accelerations develop or also in the case of water hammer. Cavitation may also occur over ship propellers and in machinery that interacts with liquid flows (pumps, turbines). The phenomenon is enhanced in case of turbulence or vortex structures because every vortex introduces a local pressure drop in the core of the vortex; this effect is identified, for example, in case of propeller blades, and in particular in the tip vortex that is usually is generated in the wake.

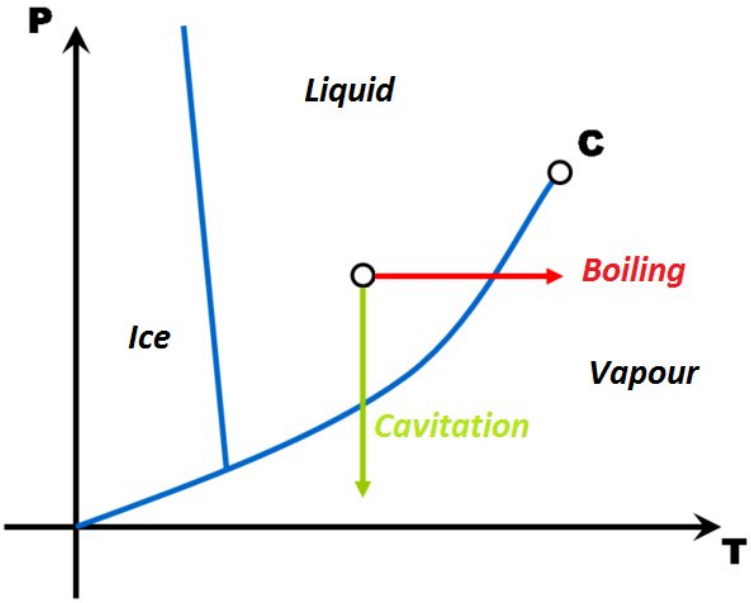

Figure 1.1: pressure-temperature phase diagram for water, with the difference between boiling and cavitation. Image taken from: `https://www.researchgate.net/figure/From-French-Wikipedia-The-well-known-phase-diagram-of-water-near-the-triple-point_fig1_313882835`

1.1.1 Cavitation types

The cause of the cavitation process is clear and its physics and dynamics may be different in different situations. The first distinction is relative to difference between traveling cavitation and fixed cavitation: The traveling cavitation, depicted in Figure 1.2, is characterized, by vapor, usually a bubble cloud with bubbles of various dimensions advected by the flow downstream until they find some higher pressure area and they condensate back to the liquid phase. Within this kind of cavitation, we can identify bubble cavitation (the vapor bubble travels along the track), or cloud cavitation if the vapor phase is almost homogeneously distributed in the fluid in that area.

This kind of cavitation is common where there is an almost homogeneous pressure drop, for example on the back of the propeller blade or in a shrinkage.

On the other hand, fixed cavitation manifests itself with the presence of a region dominated by the vapor phase, that remains in the same position, attached to some solid structures or obstacles or releasing periodically small portions of vapor. This kind of cavitation is usually related to the presence

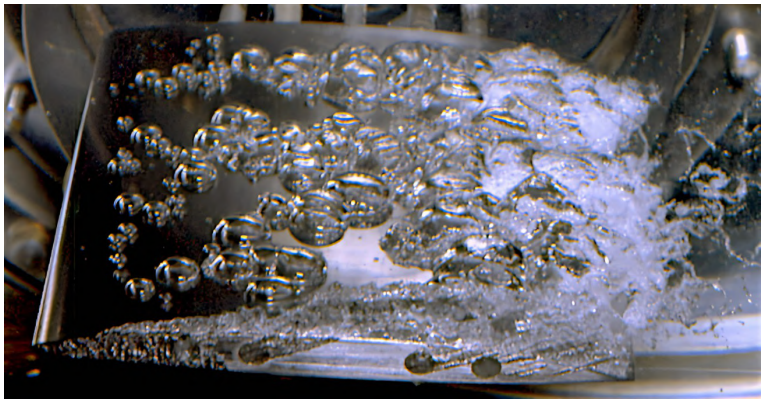

Figure 1.2: Traveling cavitation on the back of a hydrofoil. Image taken from: [Franc (2006)]

of obstacles or machinery; this kind of cavitation typically occurs within pipelines or around obstacles, as, for example, hydrofoils with a high angle of incidence.

1.1.2 cavitation for ship propellers

Cavitation is a significant problem for ship propellers and the phenomenon may appear in all its own different patterns (see Figure 1.3 for a typical example). For example, cavitation is usually found in the organized vorticity

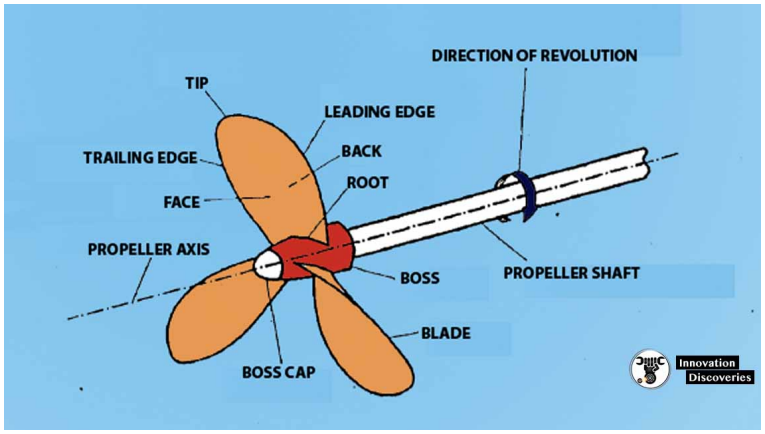

Figure 1.3: Scheme to show the parts of a ship propeller. Image taken from: `https://innovationdiscoveries.space/how-propeller-works-functions-of-propeller/`

generated by the propeller; the main vortex structures are the tip vortex released in the wake of the tip of the propeller blade or that released by

the hub. this phenomenon can be correlated to the tip vortex or the back of the blade, so we have tip vortex cavitation, or on the other side, near the propeller hub, so we will have hub cavitation; traveling cavitation could appear on the face of the blade, usually if it is working out from design conditions or in this case the angle of the blade couldn't be ideal and lead to fixed cavitation from the blade edge, called sheet cavitation.

The goal is to design the best compromize for a propeller, in terms of performance versus cavitation. In particular, propulsion performance should be obtained without obtaining a severe reduction of pressure on the back of the blade, which may lead to traveling bubble cavitation;

Also, even in case of the optimal propellers for a certain loading condition, in off-design conditions cavitation may develop, for example, in presence of rough sea, acceleration, or maneuvers where the velocity and direction of the flow do not match with the designed propeller conditions; these situations may lead to development of separated flows on the trailing edge of the blade and bring some sheet cavitation on the blade. On the tip of the blades, due to the difference of pressure between the face and the back of the blade, there will be a flow from the face to the back that generate a vortex around the tip of the blade, this particular vortex usually generated by every blade, with different intensity is called tip vortex. Sometimes, pressure in the core of this helical vortex drops below the vapor tension and generates or maintains the tip vortex cavitation. Other cavitation patterns may also be present around ship propellers and are caused by the hub or off-design conditions, as discussed above (see Figure 1.4 for an example).

1.1.3 problem of cavitation

Cavitation may represent a severe problem because of undesired effects; apart the loss of performance due to the presence of the vapour phase, problems could be related to the presence of the vapor, like the loss of performance, or related to the bubble collapse, which brings the most severe consequences.
In presence of a two-phase flow (liquid + vapor) the free-divergence (incompressibility) condition of the velocity field is no more verified; so, in presence of acceleration and associated reduction of pressure , cavitation takes place mostly on the back of a blade and occupies a large fraction of volume contributing to the reduction of the thrust causing a loss of performance of the machinery. The second, and more severe, effect is related to the cavity collapse, because usually, the condensation of vapor to liquid has almost the same dynamics as the collapse of a single vapor bubble; in this case, the bubble decreases in dimension, but when it is close to disappearing some imperfection in its spherical shape brings the bubble to microscopic flow jet

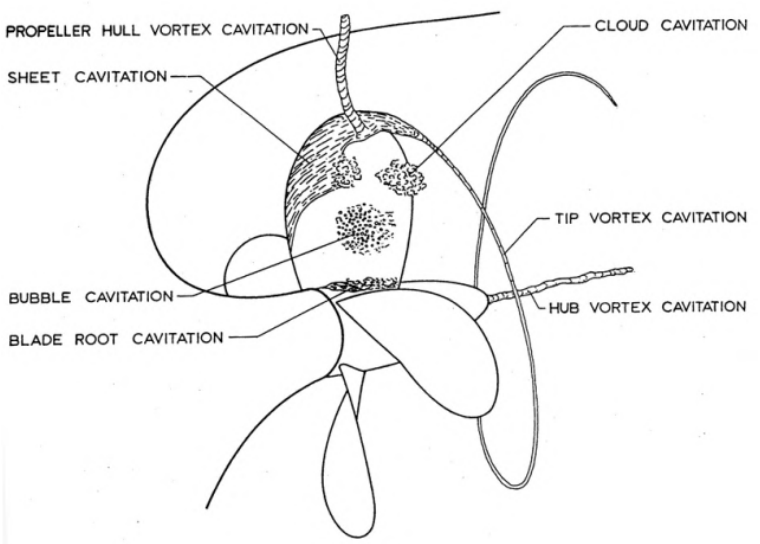

Figure 1.4: Schematic representation of the different cavitation types for a ship propeller. Image taken from: `https://www.theshipyardblog.com/propeller-cavitation-explained/`.

with velocity of hundreds of meters per seconds and very high values of pressure, locally even of the order of hundreds of atmospheres; this implosion dynamics is depicted in Figure 1.5.

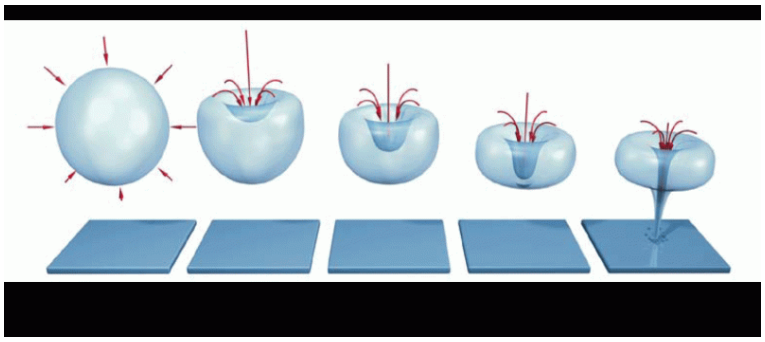

Figure 1.5: Schematic representation of the formation of the jet flow during the collapse of a vapor bubble. Image taken from: `http://massflow.ir/2018/08/14/post002`

This phenomenon is relevant also because the cavitation, and the subsequent cavity collapse, usually occur near the solid walls thus creating local erosion which sometimes brings to the collapse of the structure (see Figure 1.6).

Figure 1.6: Erosion on a propeller blade under cavitation. Image taken from: https://www.researchgate.net/publication/341131919_Numerical_Modelling_and_Prediction_of_Cavitation_Erosion_Using_Euler-Euler_and_Multi-Scale_Euler-Lagrange_Methods

Cavitation and the subsequent bubble collapse may also lead to vibrations and noise; cavitation creates noise through different mechanisms, among them, we can identify the pressure waves related to the cavity implosion, the dynamic of the cavity itself or also indirectly by the vibration induced on the structure.

1.1.4 Evaluation of cavitation

Measurement and prediction of cavitation are in general difficult, due to various problems, one of them being the different spatial and temporal scales involved in the phenomenon; as an example, the temporal scale of a single bubble is of the order of microseconds, and its characteristic dimension is of the order of few micrometers or even below smaller in presence of rebounds or implosion; The other problem when facing cavitation is the fact that it occurs in presence of very low pressure, that is tipically associated to high-speed flows in a turbulent regime, and this means that the flow is chaotic, and so also the formation and the dynamics of the bubble.

The dynamic of the vapor bubble depends on thermodynamic nonlinear mechanisms depending. For the above mentioned reasons, is is nowadays unpractical to afford cavitation by directly solving the dynamics of the single bubbles in the flow.
The mathematical models so far developed to simulate the cavitation can be classified into two main categories:

separated-flow methods, where the liquid phase and the vapor one are treated separately and separated by the interface;

dispersed-flow methods, where the two phases are treated as a mixture with spatial characteristics that change with the amount of gas present within the mixture.
In separated-flow methods, the two fluids may be solved by adopting several strategies, for example considering two separate domains, one for the liquid phase and one for the vapor phase.
Accordingly, the interface in this case works as a boundary over which specific conditions need to be set. Specifically, the pressure jump between the phases is correlated to the surface tension, while velocity is set to have the correct mass transfer through the interface, due to condensation and vaporization processes.

Also, a so-called continuous approach is suitable. In this case, one set of equations is solved, however additional terms appear in the momentum equation related to the vapor concentration. For example, introducing a Dirac delta δ_s, with which the sharp interface is intercepted.
Other methods for treating the interface are: Interface tracking or Interface capturing. Interface tracking is a Lagrangian approach where the interface points are tracked according to the velocity of the phases on neighboring cells: [Unverdi and Tryggvason (1992)]

$$\frac{\partial X_i}{\partial t} = u_i \tag{1.1}$$

The Interface capturing method does not provide for a sharp interface. Indeed, the latter may be identified as the diffused region where the flow gradually moves from one phase to the other. In this model, interface motion is evaluated by solving a transport equation:

$$\frac{\partial Y}{\partial t} + \nabla \cdot (uY) = 0 \tag{1.2}$$

Several models are present in literature and differ on the modelling strategy to determine the interface and on the meaning of the Y field ; if the Y field represents the vapor concentration, we refer to the volume of fluids methods [Brackbill et al. (1992)], if a scalar field determines the distance from the interface , we have the level set methods [Sussman et al. (1994)], or if it

is a potential of the phases we have the phase field methods [Jacqmin (1999)].

Over the years, source terms have been added to the transport equation for every model to take into account interface effects, such as mass transfer [Yang and Mao (2005), Sun et al. (2012)].

Using different fluids means tracking the liquid-vapor interface; this implies that the dimension of the computational cell should be smaller than the gas bubble dimension or the vapor structures, so these methods are widely used to study isolated bubble dynamics and are not suitable for engineering applications.

The other class of methods, called dispersed-flow methods, rely on the assumption that the flow may be treated as a mixture.
Two main models can be identified, the Euler-Euler and the Euler-Lagrangian model respectively. Recently, a merging of the two has been proposed [Ghahramani et al. (2007)], where the inception is treated considering a Lagrangian approach, while the macroscopic vapor mass dynamic is solved within an Eulerian framework.

The Euler-Lagrangian approach considers the vapor or gas as a small portion of the entire mixture so it solves the liquid problem with the Euler approach, as in equation 1.3, where u is the velocity field, P is the pressure, ρ is the density and μ is the viscosity;

$$\begin{cases} \nabla \cdot u = 0 \\ \rho \left(\frac{\partial u}{\partial t} + u \cdot \nabla u \right) = -\nabla P + \mu \nabla^2 u \end{cases} \tag{1.3}$$

while the vapor phase is treated with a Lagrangian approach: the forces on the bubble related for example to drag, shear, and buoyancy, are evaluated through the liquid-phase velocity and determine the particle trajectories. Since the model can treat a limited number of particles, it is effective to study problems related to bubble cavitation and incipient cavitation, but is not suited for cavitating flows characterized by a large amount of vapor.

On the other hand, the Euler-Euler approaches are widely in use for engineering applications.

These approaches consider the different fluids as mixed, being part of a single mixture. The dynamic of the mixture can be evaluated by solving a single set of Navier-Stokes equations, where the density and viscosity of the mixture are weighed by the vapor concentration.

The dynamic of vapor may be defined through a state equation which relates the density of the flow with the fluid dynamic pressure; these models are called barotropic models. The difference among these models is the constitutive relation $\rho = f(P)$, we mention among others the work of Del-

lannoy and Kueny, [Delannoy and Kueny (1990)], Rebound et al., [Rebound et al. (1998)], Song and He [Song and He (1998)], Coutier-Delgosha et al., [Coutier-Delgosha et al. (2005)] and Qin et al. [Qin et al. (2003)]).

Otherwise, the vapor dynamics can be evaluated by the use of a transport equation for the volume fraction of one phase. These models are based on the use of a scalar field which indicates the vapor fraction. Indeed, the characteristics of the mixture depend on the ratio between the vapor volume V_v and the total volume, evaluated as the sum of the vapor and liquid volume:

$$\alpha_v = \frac{V_v}{V_v + V_l} \tag{1.4}$$

The mixture density ρ and viscosity ν usually are evaluated through the vapor fraction α_v.

$$\rho = \rho_v \alpha_v + \rho_l \left(1 - \alpha_v\right) \tag{1.5}$$

$$\mu = \mu_v \alpha_v + \mu_l \left(1 - \alpha_v\right) \tag{1.6}$$

The transport equation accounts for the phase-change processes through the proper source/sink terms indicated with $\dot{m}$.

$$\frac{\partial \alpha_v}{\partial t} + \nabla \left(u \alpha_v\right) = \dot{m} \tag{1.7}$$

In Eq. 1.7, the source term $\dot{m}$ represents the phase change between liquid and vapor and vice versa. Since the two phenomena can be considered independent, the $\dot{m}$ term is expressed by two terms, one for condensation and one for vaporization.

$$\dot{m} = \dot{m}_v - \dot{m}_c \tag{1.8}$$

where the pedices v and c stand for vaporization and condensation respectively; the model just needs two source and sink terms to consider the contribution of the processes of vaporization and condensation: several models have been developed to parametrize these processes as a function of resolved variables; among them, we mention:

- The Merkle[Merkle et al. (1998)] model in which the source and sink terms are related to the density variation, proportional to the dynamic pressure:

$$\begin{aligned} \dot{m}_c &= C_c \frac{(1-\alpha_l)\max(p-p_v,0)}{\frac{1}{2}\rho_v U_\infty^2 t_\infty} \\ \dot{m}_v &= C_v \frac{\alpha_l \max(p_v-p,0)}{\frac{1}{2}\rho_v U_\infty^2 t_\infty} \end{aligned} \tag{1.9}$$

  where p is the pressure, p_v the vapor tension, U_∞ and t_∞ are characteristic velocity and time scales for the specific study case, while C_c and C_v are two empirical coefficients to optimize the model.

- the Kunz model [Kunz et al. (2000)] which uses the same vaporization source term as Merkle's model and a simplified Ginzburg-Landau potential for the condensation one; in this model too, the source and sink terms are separated and depend on two empirical coefficients (C_v and C_c respectively) and other fluid dynamic quantities, as the characteristic velocity and time scales U_∞, T_∞ as in the previous model.

$$\begin{aligned} \dot{m}_c &= C_c \frac{\rho}{\rho_l} \frac{\alpha_l^2(1-\alpha_l)}{t_\infty} \frac{\max(p-p_v,0)}{|p-p_v|} \\ \dot{m}_v &= C_v \frac{\rho}{\rho_l^2} \frac{\alpha_l \max(p_v-p,0)}{\frac{1}{2}U_\infty^2 t_\infty} \end{aligned} \tag{1.10}$$

- The model of Saito [Saito et al. (2007)] evaluates the source terms basing the formulation on the theory of evaporation and condensation on a plane surface:

$$\begin{aligned} \dot{m}_c &= C_c \frac{\rho}{\rho_l \rho_v} \frac{\alpha_l^2(1-\alpha_l)^2 \max(p-p_v)}{\sqrt{2\pi R T_g}} \\ \dot{m}_v &= C_v \frac{\rho}{\rho_v^2} \frac{\alpha_l^2(1-\alpha_l)^2 \max(p_v-p)}{\sqrt{2\pi R T_g}} \end{aligned} \tag{1.11}$$

  where R is the gas constant and T_g is the gas temperature

- Senocak and Shyy [Senocak and Shyy (2004)] used the mass-momentum conservation equation at the interface to evaluate the source terms as a function of known flow variables.

- Several methods base the source terms on the Rayleigh-Plesset equation for the dynamic of the bubble and are still different from each other. Among them, we find the Schnerr and Sauer model [Schnerr and Sauer (2001)] that bases the source and sink terms on the asymptotic solution of the equation for the dynamics of the bubble:

$$\begin{aligned} \dot{m}_c &= C_c \frac{3\alpha_l(1-\alpha_l)}{R_b} \sqrt{\frac{2}{3}\frac{\max(p-p_v,0)}{\rho_l}} \\ \dot{m}_v &= C_v \frac{3\alpha_l(1-\alpha_l)}{R_b} \sqrt{\frac{2}{3}\frac{\max(p_v-p,0)}{\rho_l}} \end{aligned} \tag{1.12}$$

  where the bubble radius R_b has to be evaluated also. The models contains two empirical constant to be calibrated on the particular case under investigation.

- The Zwart model [Zwart et al. (2004)] which contains a source terms dependent on the effective pressure, the vapor tension, the characteristic of the gas bubble already present in the fluid, and in particular on the concentration r_{nunc} and the initial radius R_B of the bubbles. As in

other models, the present one contains two empirical coefficients F_e, F_c.

$$\dot{m} = \begin{cases} -F_e \frac{3 r_{nunc} \rho_v}{R_B} \sqrt{\frac{2}{3} \frac{P_v - P}{\rho_L}} (1 - \alpha) & P < P_v \\ F_c \frac{3 \rho_v}{R_B} \sqrt{\frac{2}{3} \frac{P_v - P}{\rho_L}} \alpha & P > P_v \end{cases} \tag{1.13}$$

- The full cavitating model, developed by Singhal [Singhal et al. (1997)], contains the source term which depends on the kinetic energy k of the flow, on the surface tension σ, on the vapor density fraction $f_v := \alpha_v \frac{\rho_l}{\rho}$ and on two empirical coefficients C_e, C_c

$$\dot{m} = \begin{cases} -C_v \frac{k}{\sigma} \rho_l \rho_v \sqrt{\frac{2}{3} \frac{P_v - P}{\rho_l}} (1 - f_v) & P < P_v \\ C_c \frac{k}{\sigma} \rho_l \rho_l \sqrt{\frac{2}{3} \frac{P_v - P}{\rho_l}} f_v & P > P_v \end{cases} \tag{1.14}$$

An important issue related to these models is the use of empirical coefficients, which is always needed since the terms describing the condensation/vaporization processes are a simplified version of complex physical relationships. Usually, these empirical parameters C_c and C_v are calibrated for every specific problem, as for the study of the flow around a hydrofoil [Roohi et al. (2013)] or a marine propeller [Morgut and Nobile (2012)]; usually, the calibration of the coefficients is performed using optimization techniques [Zhou et al. (2019)], where the values of the coefficients are evaluated forcing the solution to obtain optimal values of some mean quantities, such as the pressure coefficient or thrust and torque coefficients, the latter in case of marine propellers.

Chapter 2

Bubble dynamics

2.1 Fundamental theory for bubbles dynamics

The formation of vapor may be viewed as a set of nuclei dispersed in the liquid (in the form of dissolved air) which react to external pressure by expanding to form visible bubbles. The radius of each bubble adjusts according to the force balance at the bubble interface. The underlying theory of bubble dynamics is presented in the fundamental work of Raileygh [Rayleigh (1917)], in which the balance of forces, internal and external to the bubble, gives rise to an ordinary differential equation for the radius of the bubble. The main assumption on which this theory is based is that the bubble remains spherical during the entire motion. The equation reads as:

$$R\frac{d^2R}{dt^2} + \frac{3}{2}\left(\frac{dR}{dt}\right)^2 - \frac{p_v - p_\infty}{\rho_l} = 0 \tag{2.1}$$

where R is the bubble radius, ρ_l is the liquid density, and p_v and p_∞ are the pressure for the bubble and the far-field respectively. Several authors extended the seminal work of Rayleigh. The most popular model to date is the one proposed by Plesset [Plesset (1949)], who introduced the effect of the surface tension at the bubble interface σ:

$$R\frac{d^2R}{dt^2} + \frac{3}{2}\left(\frac{dR}{dt}\right)^2 - \frac{p_v - p_\infty - \frac{2\sigma}{R}}{\rho_l} = 0 \tag{2.2}$$

Adding the term related to the liquid viscosity μ_l [Plesset and Prosperetti (1977)], the equation reads as:

$$R\frac{d^2R}{dt^2} + \frac{3}{2}\left(\frac{dR}{dt}\right)^2 - \frac{p_v - p_\infty - \frac{2\sigma}{R}}{\rho_l} - \frac{4\mu_l}{\rho_l R}\frac{dR}{dt} = 0 \tag{2.3}$$

The pressure inside the bubble is usually considered homogeneous and composed of a part of vapor p_v and a component of non-condensable p_g gas

that is ruled by the equation of state:

$$p_g \left(R^3\right)^k = cost \tag{2.4}$$

So the pressure inside the bubble can be expressed as:

$$P_B = p_v + p_{g,0} \left(\frac{R_0}{R}\right)^{3k} \tag{2.5}$$

where the parameter k depends on the thermodynamic transformation that is considered inside the bubble: $k = 1$ for isothermal transformations, or $k = \gamma$ for adiabatic transformations, being γ the ratio between specific heats. Equation (2.3) is the most complete equation for the isolated bubble dynamic under the hypothesis of spherical symmetry, without thermal effects and considering the surrounding flow as incompressible. Further extensions have been made to refine the Rayleigh-Plesset model, most of them collected in the work of Brennen[Brennen (1995)], among others we mention the more important for the evolution of the equation for water cavitation: in particular, the compressible liquid hypothesis in the works of Prosperetti [Prosperetti and Lezzi (1986)]; the equation for the bubble cluster proposed by Kubota [Kubota et all. (1992)]; the introduction of thermal effect introduced by Plesset and Zwicle [Plesset and Zwick (1952)].

2.2 Rayleight Plesset dimensionless equation

To investigate the dynamics of the bubble, and in particular its stability under variation of the pressure, here we consider the dimensionless Rayleigh-Plesset equation (Eq. (2.3); after neglecting thermal effects, some quantities such as σ, p_v, μ, ρ_l are constant characteristics of the fluid, so they can be considered as constant parameters.
If we multiply the equation (2.3) by the constant value $\frac{\rho_l}{p_v}$ we obtain

$$\frac{R}{R_0}\frac{\ddot{R}}{\frac{p_v}{R_0\rho_l}}+\frac{3}{2}\left(\frac{\dot{R}}{\sqrt{\frac{p_v}{\rho_l}}}\right)^2 = 1+\frac{p_{g,0}}{p_v}\left(\frac{R_0}{R}\right)^{3k}-\frac{p_\infty}{p_v}-\frac{2\sigma}{p_v R_0}\frac{R_0}{R}+4\frac{\nu}{R_0\sqrt{\frac{p_v}{\rho}}}\frac{R_0}{R}\frac{\dot{R}}{\sqrt{\frac{p_v}{\rho}}} \tag{2.6}$$

Now if define a reference radius R_0, as the value occurring in the case the far-field pressure is equal to the non-condensable pressure component $p_g - p_\infty = 0$.

$$R_0 := \frac{2\sigma}{p_v} \tag{2.7}$$

We can define the non-dimensional quantities for the dynamic of the bubble as:

$$\begin{gathered} \ddot{r} := \frac{\ddot{R}}{\frac{p_v}{R_0 \rho_l}}, \qquad \dot{r} := \frac{\dot{R}}{\sqrt{\frac{p_v}{\rho_l}}}, \qquad r := \frac{R}{R_0}, \\ \sigma^* := \frac{\sigma}{p_v R_0}, \qquad \nu^* := \frac{\nu}{R_0 \sqrt{\frac{p_v}{\rho_l}}}, \\ P^*_{g,0} := \frac{p_{g,0}}{p_v}, \qquad P^*_\infty := \frac{p_\infty}{p_v} \end{gathered} \tag{2.8}$$

Now we can rewrite the Rayleigh-Plesset equation in a dimensionless form:

$$r\ddot{r} + \frac{3}{2}\dot{r}^2 = 1 + P^*_{g,0} r^{-3k} - P^*_\infty - \frac{2\sigma^*}{r} - 4\frac{\nu^* \dot{r}}{r} \tag{2.9}$$

We can determine the equilibrium Radius R_{eq} as the solution of the steady case, thus setting $\dot{R} = \ddot{R} = 0$ in equation (2.3)

$$p_v + p_{g,0}\left(\frac{R_0}{R_{eq}}\right)^{3k} - p_\infty - \frac{2\sigma}{R_{eq}} = 0 \tag{2.10}$$

If we consider a non-condensable gas filling the bubble, the gas pressure at equilibrium $p_{g,e}$ can be determined from the equation of state:

$$p_{g,e} R_{eq}^{3k} = p_{g,0} R_0^{3k} \tag{2.11}$$

from which we can define the dimensionless pressure at the equilibrium

$$P^*_{g,e} := \frac{P_{g,e}}{p_v} = \frac{P_{g,0}}{p_v}\left(\frac{R_0}{R_{eq}}\right)^{3k} = P^*_{g,0} {R^*_{eq}}^{-3k} \tag{2.12}$$

being $R^*_{eq} = \frac{R_{eq}}{R_0}$ the non-dimensional equilibrium radius. Remembering the definition of $R_0 := \frac{2\sigma}{p_v}$, the equilibrium radius (eq. (2.10)) can be rewritten in terms of non-dimensional pressure:

$$R^*_{eq} = \frac{1}{1 + P^*_{g,e} - P^*_\infty} \tag{2.13}$$

Considering the equation (eq. (2.13)) and the state equation (2.11) we can define the equilibrium radius as a function of the far-field and equilibrium nondimensional pressures $R^*_{eq} = f\left(P^*_{g,e}, P^*_\infty\right)$.
From these considerations, we can study the equilibrium radius for the different values of pressures, considering constant values of σ, ρ_l, p_v, ν that are consistent with the case of water at a constant temperature and considering the case of an isothermal transformation for the non-condensable gas.

2.3 Static limits on P^*_∞ for the parametric study

Considering equation (2.13), to have a positive value of the equilibrium radius, the parameters have to satisfy the condition:

$$1 + P^*_{g,e} - P^*_\infty > 0 \tag{2.14}$$

To determine whether the equilibrium is stable or unstable, the sign of the second derivative of R needs to be evaluated for R close to R_{eq}. For a position close to the equilibrium, the sign of $\ddot{R}$ should be opposed to the movement, so the following condition needs to be verified:

$$\ddot{R} = f\left(\dot{R}, R\right) < 0 \quad with\, \dot{R} = 0, R = R_{eq} + \epsilon \qquad and\, \epsilon\, arbitrarily\, small \tag{2.15}$$

Linearization of the force terms in the Rayleigh-Plesset equation and evaluating it for $\left[\dot{R} = 0, R = R_{eq} + \epsilon\right]$, the condition (2.15) is equivalent to the following constraint:

$$\frac{d}{dR}\left(1 + P^*_{g,e}\left(\frac{R_{eq}}{R}\right)^{3k} - \frac{2\sigma}{R}\right)\bigg|_{R_{eq}} < 0 \tag{2.16}$$

This gives the condition:

$$\frac{2\sigma}{R_{eq}} < 3k p_{g,e} \tag{2.17}$$

Considering the calculation of the equilibrium radius (eq. 2.13)), this can be written as:

$$1 + P^*_{g,e} - P^*_\infty < 3k P^*_{g,e} \tag{2.18}$$

From the equation (2.14) and (2.18) we can define the limits for the parameter P^*_∞ to be used in the parametric study, and these are:

$$1 - (3k-1)P^*_{g,e} < P^*_\infty < 1 + P^*_{g,e} \tag{2.19}$$

2.4 Stability analysis of a bubble

This section is dedicated to the stability analysis of the Rayleigh-Plesset equation. From equation (2.10) or (2.13) we can evaluate the equilibrium radius R_{eq}, once we set the values for $P^*_{g,e}$ and P^*_∞. The equilibrium radius R_{eq} is stable if it correspond to a minimum for the potential energy function:

$$\Phi_P := \int_{R_0}^{R} -4\pi R^2 \left(p_v + p_{g,e}\left(\frac{R_{eq}}{R}\right)^{3k} - p_\infty - \frac{2\sigma}{R}\right) dR \tag{2.20}$$

Considering an isothermal behavior for the gas transformation $k = 1$, the potential energy Φ_P can be evaluated as:

$$\Phi_P := -\frac{4}{3}\pi\left(p_v - p_\infty\right)R^3 - 4\pi p_{g,e}R_{eq}^3\log(\frac{R}{R_0}) + 4\pi\sigma R^2 + C \tag{2.21}$$

Defining the adimensional potential energy $\Phi_P^* = \frac{\Phi_P}{p_v R_0^3}$; from equation (2.21) we can notice that

$$\begin{cases} lim_{R\to 0}\Phi_P^* = +\infty \\ lim_{R\to +\infty}\Phi_P^* = sign\left(P_\infty^* - 1\right)|\infty| \end{cases} \tag{2.22}$$

thus, if $P_\infty^* > 1$, R_{eq}^* is always a stable equilibrium radius. Otherwise, when $P_\infty^* < 1$, R_{eq}^* is a point of local minimum if the condition for pressure (eq. (2.18)) is verified. An example of the potential energy function for different values of $P_{g,e}^*$ and P_∞^* is depicted in Figure 2.1; three significant radii are highlighted: the equilibrium radius R_{eq}^*, the unstable equilibrium radius R_{max}^* related to the same bubble and the radius $R_{i,lim}^*$, defined as the smallest radius having the same potential energy of R_{max}^* (eq. (2.1b)). We point out that the value of R_{max}^* is the unstable equilibrium for the bubble with the same value of P_∞^* and $P_{g,0}^*$ but with another pressure value for the non-condensable gas at the equilibrium $P_{g,e}^*$. In the same way, we can notice that for every unstable equilibrium condition, the bubble with the same characteristics P_∞^* and $p_{g,0}$ has also a stable equilibrium, with a different value of $p_{g,e}$.

We performed a parametric study on the possible values for the radii $R_{max}^*, R_{i,lim}^*$, varying the parameters P_∞^* and $P_{g,e}^*$. Results are reported in Figures 2.2a and 2.2b concerning R_{max}/R_{eq} and $R_{i,lim}/R_{eq}$ respectively.

We can note in Figures 2.2a and 2.2b that the energetic results have iso-level curves that are all straight lines and they pass through the value $\left(P_{g,e}^* = 0; P_\infty^* = 1\right)$. So the ratio between the maximum radius R_{max} or the initial radius $R_{i,lim}$ with respect to the equilibrium radius R_{eq} are dependent only on one parameter that can be evaluated from P_∞^* and $P_{g,e}^*$

$$\begin{cases} \frac{R_{max}}{R_{eq}} = f\left(\frac{1-P_\infty^*}{P_{g,e}^*}\right) \\ \frac{R_{i,lim}}{R_{eq}} = f\left(\frac{1-P_\infty^*}{P_{g,e}^*}\right) \end{cases} \tag{2.23}$$

In these plots, the value of P_∞^* is limited to 1 because for $P_\infty^* > 1$ the bubble has only a stable equilibrium radius and so R_{max}^* and $R_{i,lim}^*$ are not defined. In Figures 2.2a and 2.2b we can also note that the bottom left corner of the contour is empty, since solutions of stable equilibrium are not present for those pairs $\left(P_\infty^*, P_{g,e}^*\right)$. Also, the top right corner in the Figure 2.2bdoes not have solutions because of the extreme small radius according to the mathematical relation.

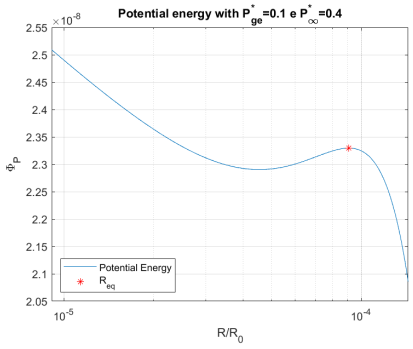

(a) $P^*_\infty < 1 - 2P^*_{g,e}$

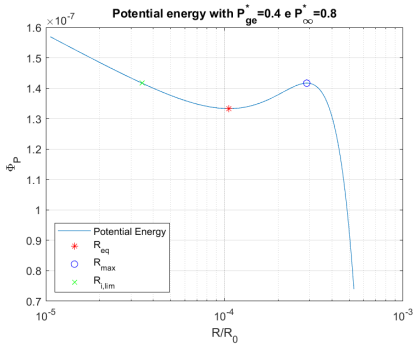

(b) $1 - 2P^*_{g,e} < P^*_\infty < 1$

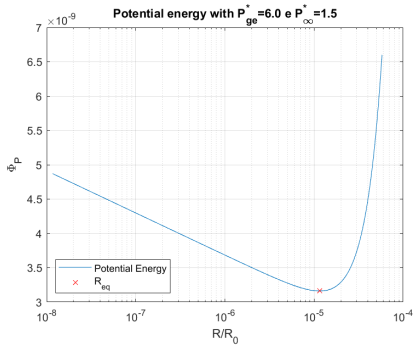

(c) $1 < P^*_\infty < 1 + P^*_{g,e}$

Figure 2.1: Potential energy function, for different values of $P^*_{g,e}$ and P^*_∞.

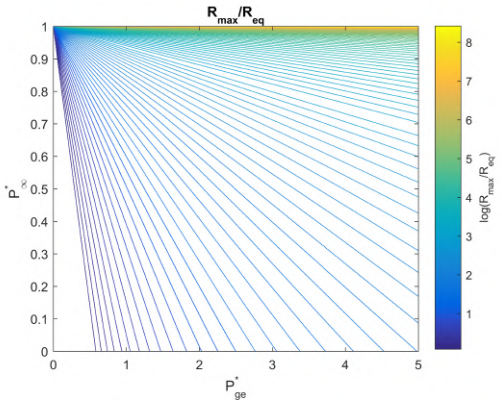

(a) R_{max}/R_{eq}

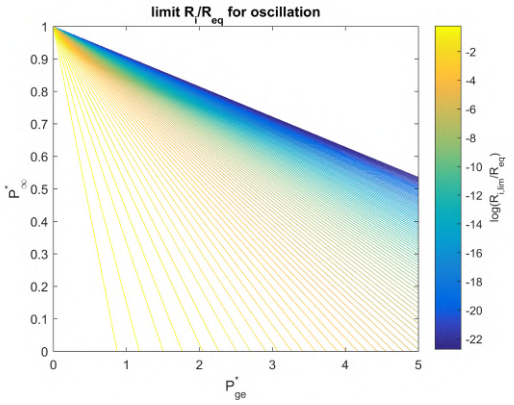

(b) $R_{i,lim}/R_{eq}$

Figure 2.2: Ratio R_{max}/R_{eq} and R_i/R_{eq}.

Finally, the relation among the three non-dimensional pressures $P^*_{g,0}$, $P^*_{g,e}$, and P^*_∞ was studied numerically with a parametric solution of the

equation

$$P^*_{g,0} = P^*_{g,e}\left(1 + P^*_{g,e} - P^*_\infty\right)^{-3k} \tag{2.24}$$

considering the value of the $k = 1$ for an isothermal transformation for the gas, and considering an interval of $P^*_{g,0} \in [0, 100]\,, P^*_\infty \in [1, 100]$. In Figure 2.3 the isocurves of $P^*_{g,0}$ are depicted.

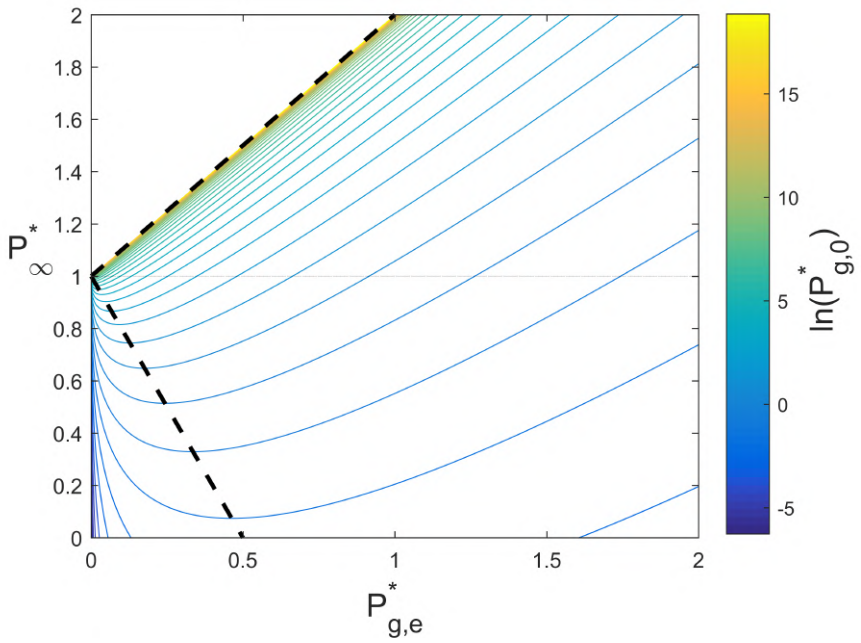

Figure 2.3: $P^*_{g,0}$ with respect to $P^*_{g,e}$ and P^*_∞.

We noticed the limits pointed out previously with the condition on the value of P^*_∞ with respect to $P^*_{g,e}$, (eq. (2.19)), indeed, the top left corner doesn't contain solutions because of the condition $P^*_\infty < 1 + P^*_{g,e}$ for the existence of the stable equilibrium radius. While in the lower part of the figure we notice that for every value of P^*_∞ there are two possible values of $P^*_{g,e}$ for every line of $P^*_{g,0}$; these two values represent the stable and unstable solutions outlined in Fig. 2.1; in particular the unstable solution is the one on the left, while the stable solution is the right one. The stable and unstable solutions are divided by the condition in equation (2.15), to be noted that the line that represents this condition crosses every $P^*_{g,0}$ isopressure curve at his minimum value.

2.5 Numerical solution of the Rayleigh-Plesset equation

In this section we describe the numerical method used for the solution of the RP equation. For this purpose, we start considering the motion of a bubble starting from a non-equilibrium situation. The first analysis concerns the numerical scheme to be used. We consider the forward Euler, an approximation of backward Euler and Heun methods, respectively, as time advance schemes.

The three methods are compared for a single bubble ruled by the Rayleigh-Plesset equation. At this stage, viscous terms are neglected and constant external pressure p_∞ is considered.
The equation, thus, reduces to:

$$R\frac{\partial^2 R}{\partial t^2} + \frac{3}{2}\left(\frac{\partial R}{\partial t}\right)^2 = \frac{p_B - p_\infty - \frac{2\sigma}{R}}{\rho_l} \tag{2.25}$$

The term for the bubble internal pressure considered is such that it describes the bubble as filled with non-condensable gas, considering isothermal transformation ($k = 1$):

$$p_B = p_v + p_{g,0}\left(\frac{R_0}{R}\right)^{3k} \tag{2.26}$$

The Rayleigh-Plesset equation can be recast considering a function that relates the acceleration of the radius $\ddot{R}$ to the radius itself R and its velocity $\dot{R}$

$$\ddot{R} = f\left(R, \dot{R}\right) = \frac{p_v + p_{g,0}\left(\frac{R_0}{R}\right)^3 - p_\infty - \frac{2\sigma}{R}}{\rho_l R} - \frac{3}{2}\frac{1}{R}\left(\frac{\partial R}{\partial t}\right)^2 \tag{2.27}$$

For the comparison of the three methods, the same parameters for the physical and numerical quantities were used, whose values are collected in Table 2.1

The first numerical method tested is the forward Euler, which computes the quantity of interest with the following discrete form:

$$q^{n+1} \approx q^n + \left(\frac{\partial q}{\partial t}\right)^n \Delta t \tag{2.28}$$

Using this approximation, the set of equations for the solution of Rayleigh-Plesset equation, assumes the form:

$$\begin{cases} R^{n+1} & = R^n + \left(\frac{\partial R}{\partial t}\right)^n \Delta t \\ \left(\frac{\partial R}{\partial t}\right)^{n+1} & = \left(\frac{\partial R}{\partial t}\right)^n + \left(\frac{\partial^2 R}{\partial t^2}\right)^n \Delta t \\ \left(\frac{\partial^2 R}{\partial t^2}\right)^{n+1} & = f\left(R^{n+1}, \left(\frac{\partial R}{\partial t}\right)^{n+1}\right) \end{cases} \tag{2.29}$$

	Symbol	Value	
Initial radius	R_0	$2 * 10^{-6}$	(m)
Time step	Δt	$1 * 10^{-8}$	(s)
Liquid viscosity	ν_l	0	$(\frac{m^2}{s})$
Liquid density	ρ_l	$1 * 10^{3}$	$(\frac{kg}{m^3})$
Tensile strength	σ	$1 * 10^{-3}$	$(\frac{N}{m^2})$
Initial bubble pressure	$p_{g,0}$	$3.17 * 10^{-6}$	$(\frac{N}{m^2})$
External pressure	p_∞	$1 * 10^{-8}$	$(\frac{N}{m^2})$

Table 2.1: Values of the physical quantities used for the comparison among the numerical methods for the bubble dynamic.

The second method that has been tested is an approximation of the backward Euler method, in which the values of the derivative for the successive time step are not evaluated implicitly because of the complexity of the equation, rather they are evaluated explicitly by using a prediction step

$$q^{n+1} \approx q^n + \left(\frac{\partial q}{\partial t}\right)^* \Delta t \tag{2.30}$$

that uses the forward Euler method; so the numerical approximation, in this case, is obtained as:

$$\begin{cases} R^* & = R^n + \left(\frac{\partial R}{\partial t}\right)^n \Delta t \\ \left(\frac{\partial R}{\partial t}\right)^* & = \left(\frac{\partial R}{\partial t}\right)^n + \left(\frac{\partial^2 R}{\partial t^2}\right)^n \Delta t \\ \left(\frac{\partial^2 R}{\partial t^2}\right)^* & = f\left(R^*, \left(\frac{\partial R}{\partial t}\right)^*\right) \end{cases} \tag{2.31}$$

and the real time-step that uses the predicted values for the next time as a derivative is

$$\begin{cases} R^{n+1} & = R^n + \left(\frac{\partial R}{\partial t}\right)^* \Delta t \\ \left(\frac{\partial R}{\partial t}\right)^{n+1} & = \left(\frac{\partial R}{\partial t}\right)^n + \left(\frac{\partial^2 R}{\partial t^2}\right)^* \Delta t \\ \left(\frac{\partial^2 R}{\partial t^2}\right)^{n+1} & = f\left(R^{n+1}, \left(\frac{\partial R}{\partial t}\right)^{n+1}\right) \end{cases} \tag{2.32}$$

The third method tested is the Heun method, which is an approximation of the semi-implicit method of Crank-Nicolson, where part of the new time step values is evaluated explicitly using a predictor step to evaluate the first iteration of the unknown values. In this case, the Euler method was adopted to evaluate the predictor step, so this method results to be the average between the forward Euler and the approximate backward Euler. In particular, the formulation in this case is:

$$q^{n+1} \approx q^n + \frac{1}{2}\left(\left(\frac{\partial q}{\partial t}\right)^{n+1} + \left(\frac{\partial q}{\partial t}\right)^n\right) \Delta t \tag{2.33}$$

And so the time advancement is carried out as in Eq. (2.31) and then the quantities are evaluated with the system:

$$\begin{cases} R^{n+1} & = R^n + \frac{1}{2}\left(\left(\frac{\partial R}{\partial t}\right)^n + \left(\frac{\partial R}{\partial t}\right)^*\right)\Delta t \\ \left(\frac{\partial R}{\partial t}\right)^{n+1} & = \left(\frac{\partial R}{\partial t}\right)^n + \frac{1}{2}\left(\left(\frac{\partial^2 R}{\partial t^2}\right)^n + \left(\frac{\partial^2 R}{\partial t^2}\right)^*\right)\Delta t \\ \left(\frac{\partial^2 R}{\partial t^2}\right)^{n+1} & = F\left(R^{n+1}, \left(\frac{\partial R}{\partial t}\right)^{n+1}\right) \end{cases} \tag{2.34}$$

The three different integration schemes were compared in the simulation of the oscillation of a single bubble with the parameters of Table 2.1 and the results are reported in Figures 2.4; we can notice that with the Euler method the radius of the bubble, after some oscillations, diverge to an infinite value, while the solution of the approximate backward method underestimates the values, in fact the radius show a damped behavior in time; finally, the Heun method, that represents the average of the first two methods, appears to model very well the dynamic of the bubble with the parameters considered.

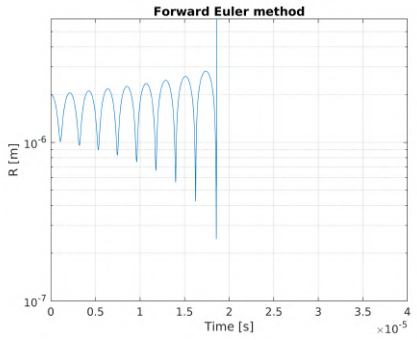

(a) Forward Euler

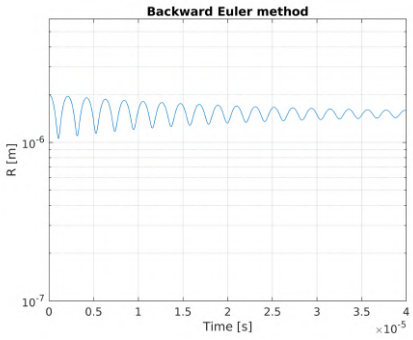

(b) Approximate backward Euler

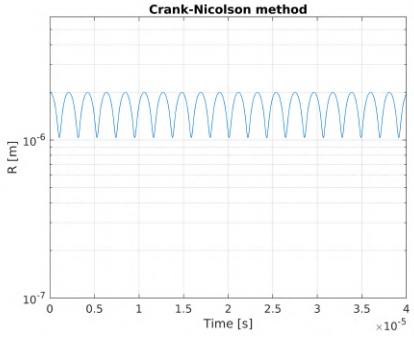

(c) Heun

Figure 2.4: Radius of the bubble during an interval using the different numerical methods.

To check the quality of the results obtained with the Heun method, an energetic balance was computed to verify the amount of energy contained in the domain during the numerical simulation. Using the hypothesis of spherical symmetry and considering the fluid as incompressible, the radial velocity at a distance r from the center of the bubble can be evaluated with the equation:

$$u_r(r) = \frac{R^2}{r^2}\dot{R} \tag{2.35}$$

So the total kinetic energy can be evaluated with the formula:

$$\begin{aligned} E_k &= \tfrac{1}{2}\rho_l \int_R^\infty r^2 u(r)^2 4\pi dr \\ &= 2\pi\rho_l R^3 \dot{R}^2 \end{aligned} \tag{2.36}$$

The potential energy can be considered as the work made by the gas at the interface during the motion from a reference radius R_0 to the radius R; so it can be evaluated as

$$\begin{aligned} E_p &= -\int_{R_0}^{R} \left(p_B - p_\infty - \tfrac{2\sigma}{R}\right) R^2 4\pi dR \\ &= -\tfrac{4}{3}\pi\left(p_v - p_\infty\right) R^3 - 4\pi p_{g,0} R_0^3 \log\left(\tfrac{R}{R_0}\right) + 4\pi\sigma R^2 + C \end{aligned} \tag{2.37}$$

We can define the total energy budget as the sum of the kinetic and potential energy $E_{tot} := E_k + E_p$ at each time. In absence of viscosity, the total energy must remain constant. In Figure 2.5 we observe that the total energy is almost constant during the simulation, except during the bubble rebounds. During these moments the numerical solver introduced some numerical errors because of the very high values of the derivatives. This errors can lead to wrong predictions of the bubble dynamics in long-time simulations.

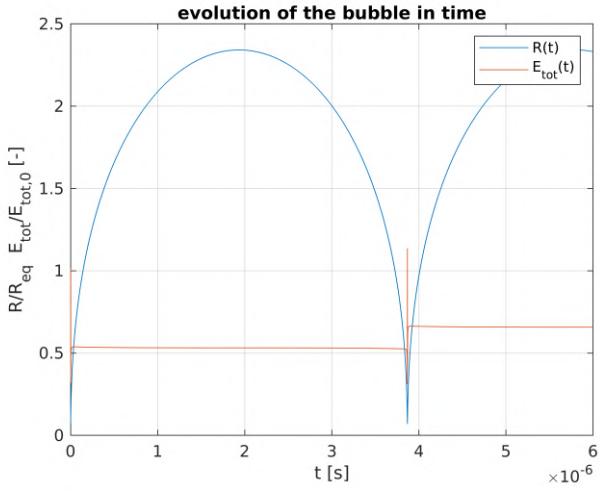

Figure 2.5: Dimensionless radius of the bubble and total energy during an interval using Crank Nicolson method.

Chapter 3

2D - flow around a cylinder

This section is dedicated to the analysis of different cavitation models. Specifically, we consider four mixture models as they are implemented in the opensource software OpenFOAM, comparing the results obtained in the case of a laminar flow around a cylinder. Standard coefficients for the condensation/vaporization terms are first considered; then, a physical-based procedure to calculate the coefficients is proposed and applied to the cylinder case.

3.1 The Multiphase Model for Flow Cavitation

The homogeneous mixture model considers the fluid composed as a mixture of two incompressible and homogeneously distributed phases. The governing equations that rule the dynamics of the mixture are the Navier-Stokes equations, together with a vapor mass transfer equation that reads as a transport equation for the vapor fraction $alpha_v$:

$$\frac{\partial \rho}{\partial t} + \nabla \cdot (\rho \mathbf{u}) = 0 \tag{3.1}$$

$$\frac{\partial \rho \mathbf{u}}{\partial t} + \nabla \cdot (\rho \mathbf{u}\mathbf{u}) = -\nabla p + \mu \nabla^2 \mathbf{u} \tag{3.2}$$

$$\frac{\partial \alpha_v}{\partial t} + \nabla \cdot (\mathbf{u}\alpha_v) = \dot{m}_v - \dot{m}_c \tag{3.3}$$

where p and $\mathbf{u}$ are the pressure and velocity fields, and the two values of ρ and μ are, respectively, the density and viscosity of the mixture and are evaluated as follow:

$$\rho = \rho_v \alpha_v + \rho_l \left(1 - \alpha_v\right) \tag{3.4}$$

$$\mu = \mu_v \alpha_v + \mu_l \left(1 - \alpha_v\right) \tag{3.5}$$

where the subscripts l and v refer to liquid and vapor phases, respectively. α_v is defined as the ratio between the volume of vapor over the total volume:

$$\alpha_v = \frac{V_v}{V_l + V_v} \tag{3.6}$$

It should be noted that in the momentum equation (3.2) the volume force term is not considered, which is equivalent to consider the hydrodynamic contribution only in the pressure term. This simplification does not affect the cavitation process in case the flow field develops over a horizontal plane. Hereafter the liquid volume fraction α_l, defined as $\alpha_l = 1 - \alpha_v$ is used. An important issue related to the homogeneous mixture method is modelization of the phase change, namely the vaporization and condensation processes, which are described by the source terms $\dot{m}_v$ and $\dot{m}_c$, in the transport equation of α_v (eq.(3.3)).

Among the available models for the phase change mechanism, in the present study we consider the following ones: the Kunz model [Kunz et al. (2000)], the Merkle model [Merkle et al. (1998)], the Saito model [Saito et al. (2007)] and the Schnerr-Sauer model [Schnerr and Sauer (2001)]. In these models, the vaporization and condensation rates $\dot{m}_v$ and $\dot{m}_c$ are always expressed as a function of the volume fraction and pressure. Saito's model was originally developed to be used in simulations where compressibility is taken into account because this model requires the solution of the energy equation as the terms of vaporization and condensation depend on temperature. Since we wotk under the assumption of incompressible flow, we need a transport equation model system without the energy equation; hence, we assume that the temperature T_g, required in the Saito model is constant both in space and time. The different expressions for the source terms of equation(3.3) of the four models are shown in Table 3.1. Please note that all terms are written for the non-conservative form of Equation(3.3).

In Table 3.1, the terms U_∞ and t_∞ are, respectively, the characteristic velocity- and time-scale of the simulation, R is the gas constant and R_b is the radius of the bubbles that is calculated runtime as a function of α_l. Differences among the models are evident and justified by the fact that they derive from different physical, empirical, or analytical considerations. In particular, we can note that except for the Schnerr-Sauer model, where the source terms depend also on the radius R_b, the two source terms $\dot{m}_v$ and $\dot{m}_c$ are polynomials of the variable α_l, of different degrees and multiplied by different coefficients. This makes the transport equation a non-linear partial differential equation. The parameters C_v and C_c, which represent vaporization and condensation coefficients, have standard literature values, (see for example [Roohi et al. (2013), Gaggero and Villa (2017), Gnanaskandan and Mahesh (2016)]). Usually, they are calibrated through optimization algorithms or by direct comparison with results from specific experiments. This may be considered a convenient although not physical-based, procedure; in-

deed, the coefficients are calibrated according to the specific application, to obtain the target value for some quantities. This procedure does not guarantee the general good performance of the model.

Model	$\dot{m}_c$	$\dot{m}_v$
Kunz	$C_c \frac{\rho}{\rho_l} \frac{\alpha_l^2(1-\alpha_l)}{t_\infty} \frac{\max(p-p_v,0)}{\lvert p-p_v\rvert}$	$C_v \frac{\rho}{\rho_l^2} \frac{\alpha_l \max(p_v-p,0)}{\frac{1}{2}U_\infty^2 t_\infty}$
Merkle	$C_c \frac{\rho}{\rho_l \rho_v} \frac{(1-\alpha_l)\max(p-p_v,0)}{\frac{1}{2}U_\infty^2 t_\infty}$	$C_v \frac{\rho}{\rho_v^2} \frac{\alpha_l \max(p_v-p,0)}{\frac{1}{2}U_\infty^2 t_\infty}$
Saito	$C_c \frac{\rho}{\rho_l \rho_v} \frac{\alpha_l^2(1-\alpha_l)^2 \max(p-p_v)}{\sqrt{2\pi R T_g}}$	$C_v \frac{\rho}{\rho_v^2} \frac{\alpha_l^2(1-\alpha_l)^2 \max(p_v-p)}{\sqrt{2\pi R T_g}}$
Schnerr-Sauer	$C_c \frac{3\alpha_l(1-\alpha_l)}{R_b} \sqrt{\frac{2}{3}\frac{\max(p-p_v,0)}{\rho_l}}$	$C_v \frac{3\alpha_l(1-\alpha_l)}{R_b} \sqrt{\frac{2}{3}\frac{\max(p_v-p,0)}{\rho_l}}$

Table 3.1: Source terms for the non-conservative form of the transport Equation (eq. (3.3)), according to the cavitation models considered.

3.2 Simulation Set up

As a test case, we consider a two-dimensional laminar flow around a cylinder. The choice of a laminar regime of a benchmark case was done to better control the fluid dynamic results, avoiding the possible contamination due to the presence of turbulence models, and with the aim to evaluate the effect of the empirical parameters to the development of cavitation. A sketch of the computational domain is shown in Figure 3.1 and details on the geometry herein considered are collected in Table 3.2.

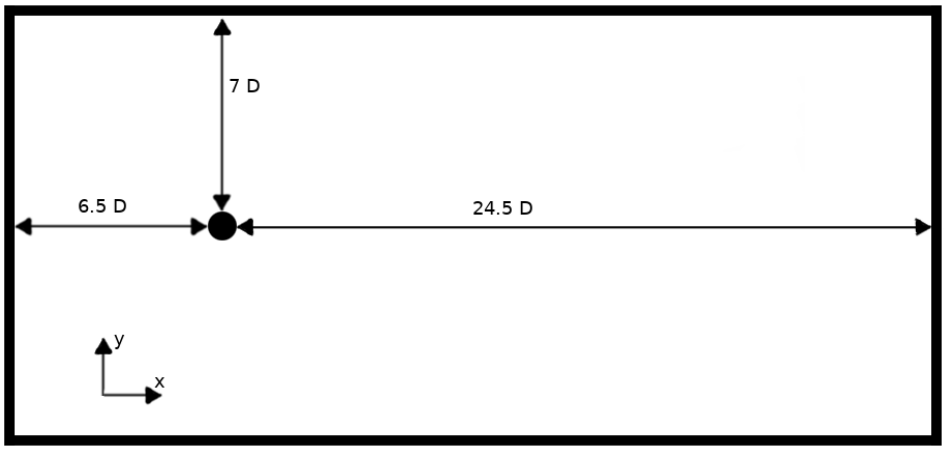

Figure 3.1: Schematic of the computational domain.

For the computational mesh, we use an unstructured grid, composed of structured blocks, with about 260,000 cells. The spatial discretization

Characteristic	Symbol	Value	
Diameter	D	1	(m)
Domain length total		32	(m)
Domain upstream length		7	(m)
Domain width		15	(m)

Table 3.2: Details on the computational domain.

is homogeneous except for stretching in the radial direction, close to the cylinder. A picture of the detail of the refined mesh is reported in Figure 3.2.

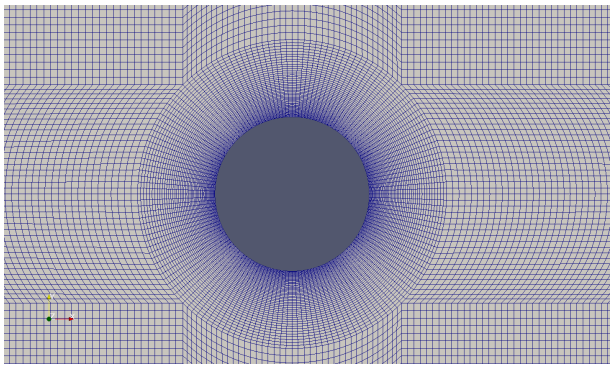

Figure 3.2: Near body mesh used for the simulations.

All simulations are carried out considering an adjustable time step, to keep the Courant number constant, but when considering the Merkle and Kunz models; in this case it was necessary to decrease the value of the Courant number, to avoid numerical instability [Lu (2008)]. We consider $Co = 0.3$ for Merkle and Kunz models, and $Co = 0.9$ for Saito and Schnerr-Sauer models.

As boundary conditions, we consider uniform velocity U_∞ and zero pressure gradient at the inlet section, on the left in Figure 3.1, while constant pressure and zero gradients for velocity are set at the outlet of the domain, on the right in Figure 3.1. Over the cylinder, a no-slip condition is imposed for the velocity field together with a zero pressure gradient condition. Symmetry conditions are imposed at the lateral boundaries. A summary of the boundary conditions of is reported in Table 3.3.

All simulations are performed in the laminar regime at Reynolds $Re = DU_\infty/\nu = 200$, based on the cylinder diameter $D = 1$ m and the uniform inlet velocity $U_\infty = 1$ m/s. At this value of Re, a Von Karman vortex street is observable and characterized by a value of Strouhal number approx 0.2. The cavitation index is $\sigma = (p_0 - p_v) \,/\, /(0.5\rho_l U_\infty^2) = 0.7$, where p_0 is the imposed output pressure; this corresponds to one of the cases analyzed

Boundary	$\boldsymbol{\alpha_l}$	u	$\boldsymbol{p}$
Inlet	uniform 0.99	uniform $(1, 0)$ m/s	zero gradient
Outlet	zero gradient	zero gradient	uniform 2650 Pa
Cylinder	zero gradient	uniform 0 m/s	zero gradient
Lateral boundaries	zero gradient	zero gradient	zero gradient

Table 3.3: Boundary conditions for the simulation of the two-dimensional laminar flow around the cylinder.

in [Gnanaskandan and Mahesh (2016)]. Table 3.4 summarizes the physical quantities considered in all simulations.

Characteristic	Symbol	Value	
Reynolds number	Re	200	(-)
Cavitation index	σ	0.7	(-)
Liquid density	ρ_l	1000	(kg/m^3)
Liquid kinematic viscosity	ν_l	0.005	(m^2/s)
Vapor density	ρ_v	0.023	(kg/m^3)
Vapor kinematic viscosity	ν_v	2.374	(m^2/s)
Vapor pressure	p_v	2300	(Pa)
Input velocity	U_∞	1	(m/s)
Output pressure	p_0	2650	(Pa)

Table 3.4: Fluid data considered in simulations.

Other parameters and coefficients which characterize the cavitation models (see Table 3.1 for the source terms description) are reported in Table 3.5.

Characteristic	Symbol	Value	
Velocity	U_∞	1	(m/s)
Reference time	t_∞	1	(s)
Gas costant	R	461.6	(J/(Kg K))
Temperature	T_g	300	(K)
Free nuclei density	n	$1.6 * 10^{13}$	(1/m^3)
Free nuclei diameter	d_{nuc}	$2 * t10^{-6}$	(m)

Table 3.5: Set up of parameters contained in the cavitation models.

The simulations were performed using a serial version of the code, which requires approximately 6 h of computer time for the 100 seconds of simulations using the Schnerr-Sauer model.

Simulations were performed using OpenFOAM's interPhaseChangeFoam solver, which uses a PIMPLE algorithm; time derivatives are evaluated using an explicit Euler scheme while various numerical schemes are used for

the spatial derivatives, the linear upwind scheme is used for the velocity divergence and a Gauss-Van Leer scheme is used for the liquid volume fraction divergence; non-orthogonal correction is considered within the Gauss linear scheme for the computation of the Laplacian.

3.3 Results with standard coefficients

In this section, we compare the results of the simulations of the laminar flow around the cylinder, obtained considering the four cavitation models with some standard literature coefficients reported in Table 3.7; we compare our results also with those of the laminar case at $Re = 200$ of the numerical study of [Gnanaskandan and Mahesh (2016)].

We classify the cavitation types observed in our numerical experiments in three regimes:

- Cyclic regime, occurring when the cavity periodically detaches from the body at the shedding frequency;
- Fixed regime, occurring when the cavity at the rear of the cylinder is stable and small vapor spots occasionally detach;
- Transitional regime, occurring when both previous regimes occur alternatively.

In [Gnanaskandan and Mahesh (2016)], the authors observed both the first and the third regime. In particular, the cyclic regime was observed at $\sigma = 1.0$ and the transitional regime at $\sigma = 0.7$ and 0.5. The latter regime is characterized by a low-frequency cavity detachment, in addition to the shedding frequency. On the other hand, a flow around bluff bodies exhibits also the fixed regime [Fry (1984), Matsudaira et al. (1992)]. In our simulations, we rarely observe the cavity that forms behind the cylinder to be completely attached to the body. However, it remains stable over time in correspondence with the recirculation areas behind the cylinder.

Figure 3.3 shows snapshots of α_l for the simulation carried out with the Kunz model with the standard coefficients reported in Table 3.7. During the simulation two alternative scenarios are identified; the first one is the detached cavitation, as depicted in Figure 3.3a, characterized by two vapor zones that oscillate downstream the cylinder; the second scenario is the formation and collapse of an attached cavity at the rear of the cylinder, as depicted in Figure 3.3b–h where downstrem advection of vapor spots is observable within the vortex cores. This scenario begins with the detachment of cavities from the cylinder (Figure 3.3b), they are advected downstream while new vapor forms near the cylinder (Figure 3.3c,d). The new cavities merge into a single cavity at the rear of the cylinder (Figure 3.3e,f). The

cavity slowly condenses maintaining the position near the cylinder but reducing its extension (Figure 3.3f,g) until the occurrence of complete collapse and the stable detached cavitation is recovered (Figure 3.3i).

(**a**) $tD/U_\infty = 43$.

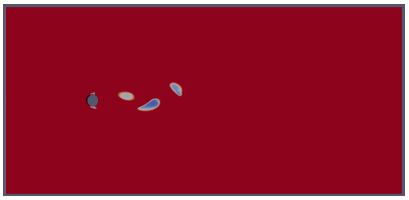

(**b**) $tD/U_\infty = 59$.

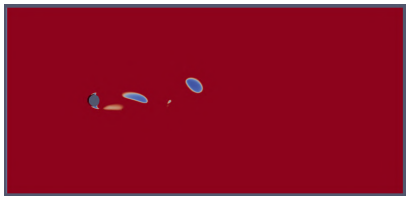

(**c**) $tD/U_\infty = 61$.

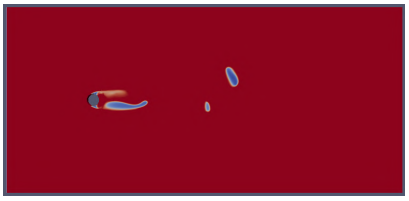

(**d**) $tD/U_\infty = 65$.

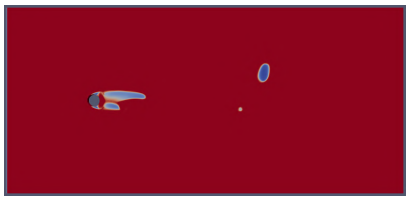

(**e**) $tD/U_\infty = 68$.

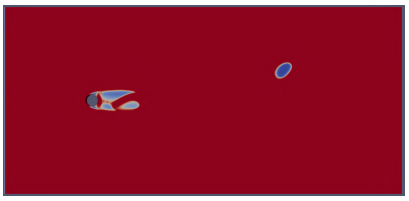

(**f**) $tD/U_\infty = 70$.

(**g**) $tD/U_\infty = 72$.

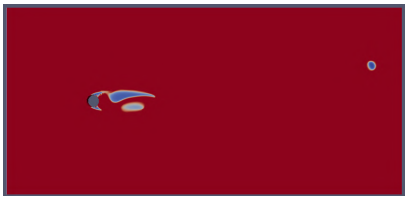

(**h**) $tD/U_\infty = 78$.

(**i**) $tD/U_\infty = 83$.

Figure 3.3: Contour plot of instantaneous liquid fraction obtained with Kunz model and considering standard coefficients.

The simulation carried out with the Merkle model (Figure 3.4) depicts cavity dynamics comparable to that obtained with the Kunz model, except for the cavity size, which is in general larger than that found with the Kunz model (Figure 3.4a); the formation of the attached cavity is visible in Figure 3.4c,d and it appears larger than the one shown in Figure 3.3e–g.

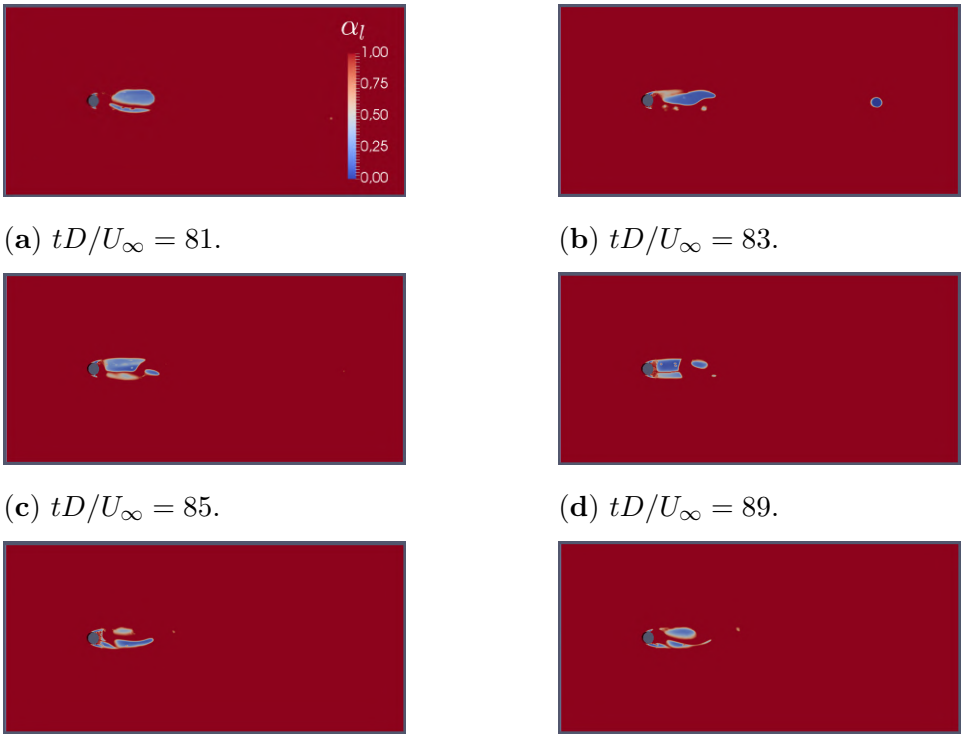

(**a**) $tD/U_\infty = 81$. (**b**) $tD/U_\infty = 83$.

(**c**) $tD/U_\infty = 85$. (**d**) $tD/U_\infty = 89$.

(**e**) $tD/U_\infty = 94$. (**f**) $tD/U_\infty = 95$.

Figure 3.4: Contour plot of instantaneous liquid fraction, results obtained with Merkle model and considering standard coefficients.

Figure 3.5 shows snapshots of the simulation performed with the Saito model, considering the standard coefficients. In this case, the cyclic regime is clear. Indeed, the regular formation of the attached cavity is ruled by vortex shedding, which is nearly unaffected by the small amount of cavitation produced by the model.

Figure 3.6 shows snapshots of the quantity α_l for the simulation performed with the Schnerr-Sauer model. The results show an alternating vapor formation downstream of the cylinder as depicted in the snapshots Figure 3.6a–c, and the occurrence of extended vaporization at the rear of the body (Figure 3.6d–i). Figure 3.6d–f shows the development of the attached cavity which occurs starting from the cylinder unlike the simulations with the Kunz (Figure 3.3) and Merkle (Figures 3.4) models, where the cav-

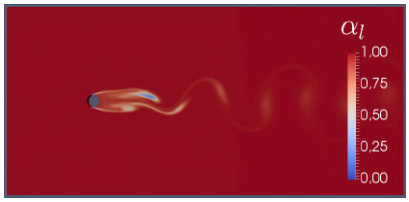

(**a**) $tD/U_\infty = 62$.

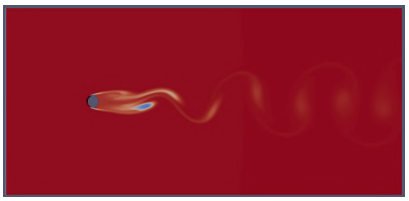

(**b**) $tD/U_\infty = 65$.

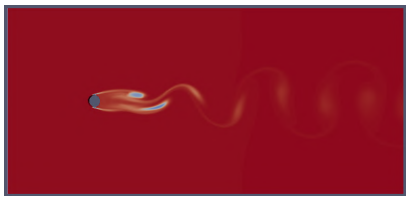

(**c**) $tD/U_\infty = 68$.

Figure 3.5: Contour plot of instantaneous liquid fraction, results obtained with Saito model and considering standard coefficients.

ity is formed in the vortex cores. Figure 3.6g–i shows that the vapor cavity at the rear of the cylinder, obtained with the Schnerr-Sauer model, is more stable and remains attached to the cylinder for a longer period if compared to the other models.

In Figure 3.7, contours of time-averaged α_l are depicted. No particular differences are detected in the shape of the mean cavity. However, the Saito model and, to a minor extent the Kunz model, produces a smaller amount of vapor compared to the other models.

Figure 3.8 contains the mean vapor fraction plotted along the centerline, downstream the cylinder. The minimum of α_l obtained with the Saito model is about $\alpha_{l,min} = 0.86$. On the other hand, the Saito model produces a longer attached cavity. This means that, unlike the other models, the low condensation rate allows the flow to carry downstream the small amount of vapor produced by the model. This behavior is expected since the vaporization and condensation rates of the Saito model maintain in time a very low value (see the α_l growth and decrease in time, depicted in Figures 3.12). The results obtained with Merkle and Schnerr-Sauer models are comparable with each other, due to their similar vaporization and condensation rates. Finally, the Kunz model stands in the middle between the Saito and the others. Indeed, it does not produce a considerable amount of vapor.

Figure 3.9 shows the profile of $\langle u'u' \rangle / U_\infty^2$ evaluated along the centerline, downstream the cylinder, being $u' = u - \langle u \rangle$ the fluctuation of the stream-wise velocity component with respect to the time-averaged value (the brackets denote an averaging operation).All models exhibit the same behavior, characterized by a single peak located roughly at the same posi-

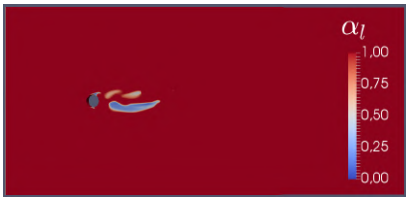

(**a**) $tD/U_\infty = 76$.

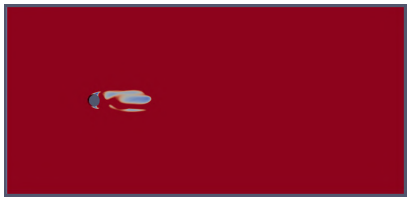

(**b**) $tD/U_\infty = 78$.

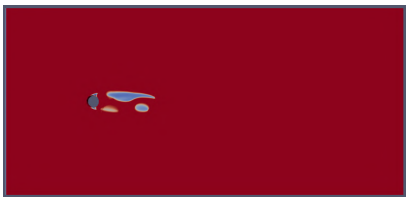

(**c**) $tD/U_\infty = 81$.

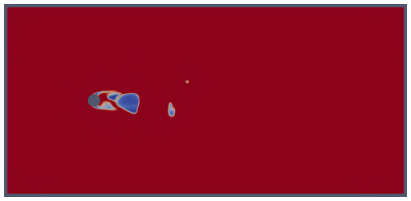

(**d**) $tD/U_\infty = 32$.

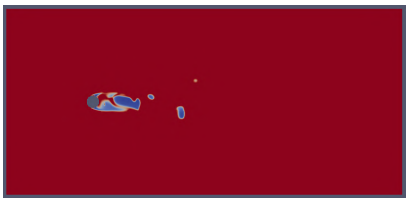

(**e**) $tD/U_\infty = 33$.

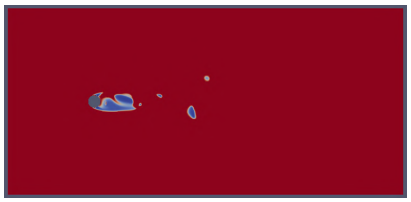

(**f**) $tD/U_\infty = 34$.

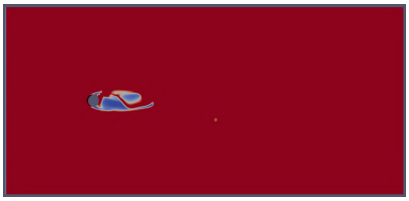

(**g**) $tD/U_\infty = 50$.

(**h**) $tD/U_\infty = 54$.

(**i**) $tD/U_\infty = 57$.

Figure 3.6: Contour plot of instantaneous liquid fraction, results obtained with SchnerrSauer model and considering standard coefficients.

tion, except for the Saito model which presents a peak slightly closer to the cylinder. This is consistent with what was observed in [Gnanaskandan and

Mahesh (2016)] since a cyclic regime exhibits a vortex shedding similar to the single-phase case, in which the re-attachment point (where $\langle u'u' \rangle / U_\infty^2$ is maximum) is closer to the cylinder in case of cavitation. Furthermore, at the rear of the cylinder $\langle u'u' \rangle / U_\infty^2$ is similar for all models except for the Saito one, which has a lower initial slope. This difference can be explained by the cyclic cavitation regime, in which cavitation has little influence on the vortex shedding, and occurs mainly in the vortex core; in the parametric study of [Gnanaskandan and Mahesh (2016)] it is noted that as σ decreases from $\sigma = 1$ to $\sigma = 0.5$ the space derivative of $\langle u'u' \rangle / U_\infty^2$ near the cylinder increases, and the value of the peak changes from a value of about 0.035 to 0.1 with a peak position ranging from $3D$ to $7.5D$; while for values of $\sigma = 0.7$ the authors find that the peak is at a position of 4.5 D with a maximum value of about $\langle u'u' \rangle / U_\infty^2 = 0.07$. The results shown in Figure 3.9 are consistent with the cavitation regimes depicted in the snapshots of the contour of α_l. Indeed the Saito model, which is the only one that exhibits a cyclic regime, is the one with a lower peak, which is also closer to the cylinder, than the other models. Conversely, the Schnerr-Sauer model, which is the one producing the most stable attached cavity, has the peak of α_l with the highest value.

(**a**) Kunz model.

(**b**) Merkle model.

(**c**) Saito model.

(**d**) Schnerr-Sauer model.

Figure 3.7: Contour plot of time-averaged liquid fraction, results obtained considering standard coefficients.

Figure 3.10 shows the spectra of the lift coefficient time-history, which gives important information about the frequency of the vortex release. In the present case, broad-band spectra appear and they differ from model to

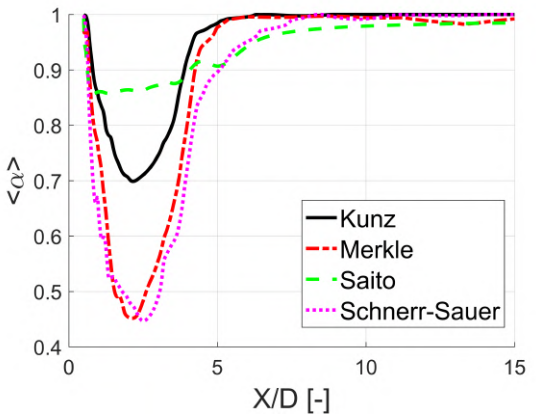

Figure 3.8: Mean liquid fraction downstream the cylinder along the centerline, results obtained considering standard coefficients.

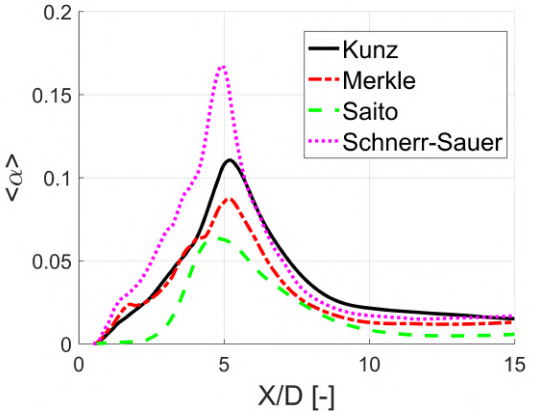

Figure 3.9: Variance of stream-wise velocity component downstream the cylinder along the centerline, results obtained considering standard coefficients.

model. This is not surprising, since the dynamics of the cavity behind the cylinder affect the flow field. We note that both the Kunz and Saito models exhibit a well-defined main peak at $St = fD/U_\infty \sim 0.15$, which is smaller than the value obtained in the single-phase regime; the Merkle and Schnerr-Sauer models give higher values of St for the peak of C_L and broad-band spectra are evident that may be due to pressure fluctuations in the presence of the attached cavity. Given the previous observations (especially about the profile of the time-averaged α_l depicted in Figure 3.8) this is reasonable, in the sense that the low amount of vapor produced by the Kunz and Saito

models, slightly affects the oscillatory pattern behind the cylinder.

In Figure 3.11, we report the mean pressure field evaluated over the cylinder surface, related to the four models. We compare our results to those reported in [Gnanaskandan and Mahesh (2016)]. In Figure 3.11 we refer to the local σ, which is defined as $\sigma_{loc} = (\bar{p} - p_v) \,/\, \left(0.5\rho_l U_\infty^2\right)$ as a function of θ, defined as the angular coordinate of the cylinder surface, where $\theta = 0$ and $\theta = 180$ are the leading edge and the trailing edge, respectively. It appears that in our simulations the incipient cavitation point is shifted a little further upstream than in the reference case [Gnanaskandan and Mahesh (2016)]. It is also noted that the pressure value upstream the cylinder is slightly different among the various cases and from the reference value. This may be due to the fact that we use pressure boundary conditions different from those of [Gnanaskandan and Mahesh (2016)], where the authors imposed the free-stream pressure on all far-field boundaries; we recall that in our cases the pressure is imposed at the outlet. In our simulations, we observe significant pressure fluctuations making σ_{loc} positive, just a little further downstream of the incipient cavitation point. The pressure fluctuations are found to be associated with the collapse of vapor spots and the variation of the cavity shape.

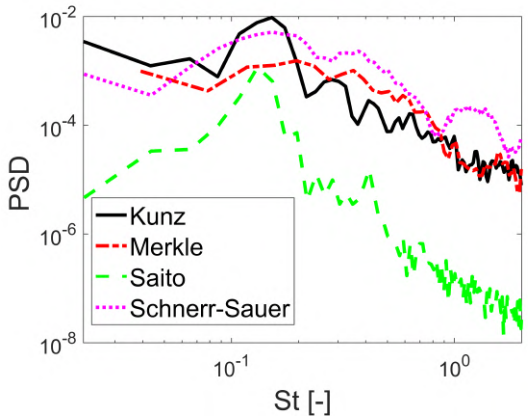

Figure 3.10: Lift coefficient, results obtained considering standard coefficients (Table 3.7).

To quantify the differences observed among the models, we consider the length of the attached cavity, the length of the vortex formation, and the vortex shedding frequency. The length of the attached cavity is defined as the position along the centerline where the vapor fraction exceeds the threshold value $\alpha_l = 0.95$. The length of the vortex formation is defined as the position along the centerline where $\langle u'u' \rangle / U_\infty^2$ reaches the maximum value. The vortex shedding frequency is defined as the frequency associated with the main peak, considering the spectrum of the lift coefficient C_L. All quantities

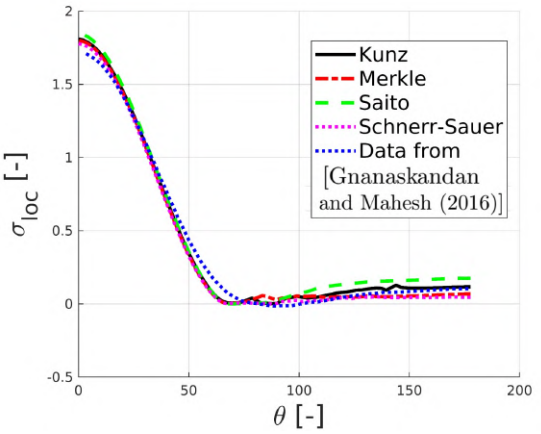

Figure 3.11: Mean pressure on the cylinder surface, results obtained considering standard coefficients (Table 3.7).

are evaluated considering the results of Figures 3.8–3.10. In [Gnanaskandan and Mahesh (2016)], the authors found that for $\sigma = 0.7$, the minimum value of the mean liquid fraction is about 0.8 with an attached cavity length of about $5\,D$.In our study, we find that the length of the attached cavity varies within the range $[4.1\,D, 6.3\,D]$ being the minimum of mean liquid fraction $\alpha_{l,max}$ in the range $[0.45, 0.85]$. The variance exhibits peaks in the range $\left(\langle u'u'\rangle/U_\infty^2\right)_{max} \in [0.06, 0.17]$, located at distances varying from $4.7\,D$ to $5.2\,D$.

In Table 3.6, we report the length of the attached cavity, the vortex formation length, and the vortex shedding frequency, related to the four models.

Model	**Mean Length of Attached Cavity**	**Vortex Formation Length**	**Vortex Shedding Frequency**
Kunz	$4.17\,D$	$5.20\,D$	0.149
Merkle	$4.63\,D$	$5.15\,D$	0.240
Saito	$6.24\,D$	$4.68\,D$	0.134
Schnerr-Sauer	$5.98\,D$	$4.93\,D$	0.165

Table 3.6: Length of the attached cavity, vortex formation length, and non-dimensional vortex shedding frequency. Results obtained considering standard coefficients.

To summarize, results show that although the time-averaged liquid fraction does not exhibit noticeable differences among models, the snapshots and the other quantities above reported reveal a substantially different be-

havior of the cavitation. The Saito model is characterized by low values of vapor fraction which do not affect the flow field, rather they are affected by it, being transported downstream. This is identified as a cyclic regime. The Schnerr-Sauer model seems to be the one that has the most stable attached cavitation alternating with periods of detached cavitation, exhibiting a well-defined transitional regime. Merkle and Kunz models behave similarly, having predominantly detached cavitation, with some phases of attached cavitation but very unstable and of short duration.

3.4 Condensation/Vaporization Coefficients normalization

A typical outcome of the transport equation models is that, using different cavitation models with standard literature coefficients, the space-time distribution of the vapor phase may differ from case to case, as clearly visible and discussed in the previous section 3. In this section, we propose an analytical computation of the multiplying factors C_c and C_v of the source terms of the vapor transport equation that can be considered a normalization procedure. Indeed, we consider a reference time scale for the vaporization-condensation processes, to normalize the coefficients of the different models. In the models, the role of the coefficients C_c and C_v consists in accelerate or decelerate the vaporization and condensation processes, thus the choice of a reference integral time scale is needed as a condition for the calculation of these coefficients. Since we don't have available experimental data for the vaporization or condensation in a controlled environment, the reference integral time scale T_{ref} that we consider is obtained through the Schnerr-Sauer model, by setting its coefficients $C_c = C_v = 1$. This aspect can be revised and improved, for example by considering a reference time T_{ref} obtained from laboratory tests or taking advantage of literature research. We calculate the coefficients C_c and C_v related to the three cavitation models (Kunz, Merkle, and Saito) such that the transition time from $\alpha = 0.9$ to $\alpha = 0.1$ takes place exactly in the time interval T_{ref}. Doing that, the models are designed to provide the same vaporization and condensation rate. From the theory of the bubble dynamic, which is the basis for the Schnerr-Sauer model, the two reference times for the condensation and the vaporization have the same value; conversely, for example, in [Garamani et al. (2021)], the authors used a condensation coefficient smaller than the vaporization one, because of different time scales of the two processes, based on experimental and empirical consideration; so the choice of two different time scales may better represent the processes.

The time evolution of α given by the different source terms is first analyzed neglecting the advective term and considering a constant pressure drop $\Delta p = p - p_v = 1\,Pa$. First, we show the time evolution of α obtained

with the standard values of the coefficients (Table 3.7) used in the previous section 3 for comparison purposes; vaporization and condensation are, respectively, in the left panel and the right panel of Figure 3.12.

Model	C_c	C_v
Kunz	1000	1000
Merkle	80	$1 * 10^{-3}$
Saito	0.1	0.1
Schnerr-Sauer	1	1

Table 3.7: Standard coefficients.

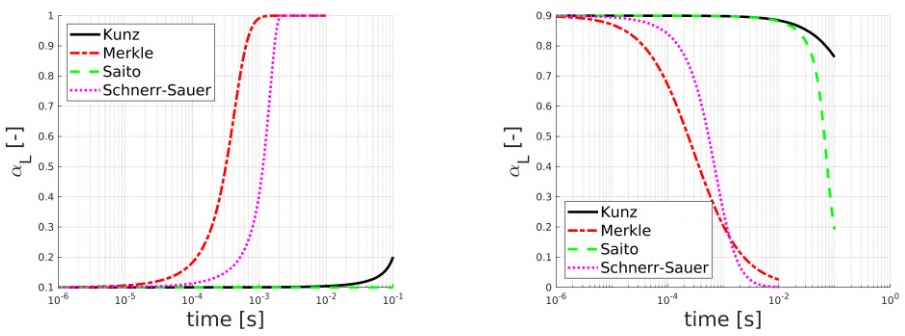

(a) Condensation process (b) Vaporization process

Figure 3.12: Condensation (left panel) and vaporization (right panel) processes, evaluated with standard coefficients.

The models exhibit substantially different behavior. It is worth noting the different values of the local time derivative, at cavitation inception (looking at low values of α in the left panel) and at incipient condensation ($\alpha \sim 1$ in the right panel); even more important is the differences in the time interval needed for a complete change of phase (either condensation or evaporation). To summarize, the standard values of the coefficient used in the models produce different time scales for the complete condensation/vaporization processes. It should be noted that we use a semi-log plot to better visualize all profiles, and even in this case, the vaporization for the Kunz model is not visible in the plot, like also the condensation for the Kunz model, and even more for the Saito model.

To obtain the reference time T_{ref} needed for the coefficients normalization, we integrate the simplified transport equation of α_v in case of $\mathbf{u} = 0\,[m/s]$. We define the time interval $T_{ref} = [t_0, t_1]$ such that the mixture evolves from an initial vapor fraction $\alpha\,(t_0) = \alpha_0$ to his final value $\alpha\,(t_1) = \alpha_1$; it's worth noting that some models have dependencies on the

vapor fraction that not allow considering the complete interval of $\alpha \in [0,1]$; so we decided to consider the interval, $\alpha_0 = 0.1$ and $\alpha_1 = 0.9$. It is important to point out that the choice of the interval $[\alpha_0, \alpha_1]$ is somewhat arbitrary, and further studies are needed to investigate how the integration interval may affect the results. Moreover, different intervals for the two phases, vaporization and condensation, should be tested, because the two processes may have different time scales.

We integrate the transport equation as follows:

$$T_{ref} = \int_{\alpha_0}^{\alpha_1} \left(\frac{1}{\dot{m}_v - \dot{m}_c} \right) d\alpha \tag{3.7}$$

Since in the mixture model the two terms $\dot{m}_v$ and $\dot{m}_c$ are not simultaneously active we can consider separately the computation of the reference time scale for the vaporization and the condensation processes;

$$T_{c,ref} = \frac{1}{C_c} \int_{\alpha_0}^{\alpha_1} \frac{1}{m_{Dest}} d\alpha \tag{3.8}$$

$$T_{v,ref} = \frac{1}{C_v} \int_{\alpha_0}^{\alpha_1} \frac{1}{m_{Prod}} d\alpha \tag{3.9}$$

where we define the terms m_{Dest} and m_{Prod} such that

$$\dot{m}_c = C_c m_{Dest} \tag{3.10}$$

$$\dot{m}_v = C_v m_{Prod} \tag{3.11}$$

Finally, the coefficients read as:

$$C_c = \frac{\int_{\alpha_0}^{\alpha_1} \frac{1}{m_{Dest}} d\alpha}{T_{c,ref}} \tag{3.12}$$

$$C_v = \frac{\int_{\alpha_0}^{\alpha_1} \frac{1}{m_{Prod}} d\alpha}{T_{v,ref}} \tag{3.13}$$

The analytical results of the integral $\int_{\alpha_0}^{\alpha_1} \frac{1}{m_{Dest}} d\alpha$ and $\int_{\alpha_0}^{\alpha_1} \frac{1}{m_{Prod}} d\alpha$ for the four models considered (Kunz, Merkle, Saito, and Schnerr-Sauer) are collected in Table 3.8. In the Table $k := \frac{\rho_l - \rho_v}{\rho_v}$ just to write the equation more clearly.

In our study, the reference times $T_{c,ref}, T_{v,ref}$ related to condensation and vaporization processes, required to evaluate the coefficients, are taken from the Schnerr-Sauer model. In particular, equations (3.8) and (3.9) are used to calculate the times $T_{c,ref}$ and $T_{v,ref}$ setting $C_c = C_v = 1$. The values of $T_{c,ref}$ and $T_{v,ref}$ are then used in Equations (3.12) and (3.13) to calculate the new coefficients for the other models.

model	$\int_{\alpha_0}^{\alpha_1} \frac{1}{m_{Prod}} d\alpha$ $\int_{\alpha_0}^{\alpha_1} \frac{1}{m_{Dest}} d\alpha$
Kunz	$\frac{\frac{1}{2}\rho_l^2 U_\infty^2 t_\infty}{\rho_v \Delta p} \left[\log(\alpha) - \log(k\alpha+1)\right]_{\alpha_0}^{\alpha_1}$ $\frac{\rho_l t_\infty}{\rho_v} \frac{\max(p-p_v,\varepsilon)}{\Delta p} \left[\frac{k^2 \log(k\alpha+1)}{k+1} - k\log(\alpha) - \frac{\log(1-\alpha)}{k+1} - \frac{1}{\alpha} + \log(\alpha)\right]_{\alpha_0}^{\alpha_1}$
Merkle	$\frac{\frac{1}{2}\rho_v U_\infty^2 t_\infty}{\Delta p} \left[\log(\alpha) - \log(k\alpha+1)\right]_{\alpha_0}^{\alpha_1}$ $\frac{\frac{1}{2}\rho_l U_\infty^2 t_\infty}{\Delta p} \left[\frac{\log(k\alpha+1)-\log(\alpha-1)}{k+1}\right]_{\alpha_0}^{\alpha_1}$
Saito	$\frac{\rho_v^2\sqrt{2\pi RT}}{\rho_l \Delta P} \left[\frac{1}{1-\alpha} - \frac{1}{\alpha} - 2\log(1-\alpha) + 2\log(\alpha)\right]_{\alpha_0}^{\alpha_1}$ $\frac{\rho_v\sqrt{2\pi RT}}{\Delta P} \left[\frac{1}{1-\alpha} - \frac{1}{\alpha} - 2\log(1-\alpha) + 2\log(\alpha)\right]_{\alpha_0}^{\alpha_1}$
Schnerr-Sauer	$\sqrt{\frac{\rho_l}{6\Delta p}} \sqrt[3]{\frac{4}{3}\pi n_{nuc}} \left[-3\sqrt[3]{\frac{1}{\alpha}-1}\right]_{\alpha_0}^{\alpha_1}$ $\sqrt{\frac{\rho_l}{6\Delta p}} \sqrt[3]{\frac{4}{3}\pi n_{nuc}} \left[-3\sqrt[3]{\frac{1}{\alpha}-1}\right]_{\alpha_0}^{\alpha_1}$

Table 3.8: Analytical integration of the reciprocal of the source terms in α.

After evaluation of the integrals of equations (3.12) and (3.13), reported in Table 3.8, we obtain the values for the analytical-based values for the coefficients that are reported in Table 3.9.

TO be noted that we consider a cavitation number $|p-p_v|/\left(0.5\rho_l U_\infty^2\right) = 2*10^{-3}$ given by the chosen pressure drop $\Delta p = |p-p_v| = 1\,[Pa]$.

Model	C_c	C_v
Kunz	$4.11*10^4$	$2.91*10^6$
Merkle	$3.33*10^1$	$1.55*10^{-3}$
Saito	$3.75*10^5$	8.66
Schnerr-Sauer	1	1

Table 3.9: Analytical-based coefficients.

The time evolution of the vapor fraction computed considering the normalized coefficients reported in Table 3.9, with the simplified transport equation are depicted in Figure 3.13.

It can be observed that although the target values α_0 and α_1 are reached at the same time $T_{c,ref}$ and $T_{v,ref}$, still the time evolution of α depends on the characteristics of the model. This makes clear the difficulty of obtaining complete homogeneity between the various models even with this calibration procedure.

It should be noted that the spatial distribution of the mean liquid fraction and the variance of the stream-wise velocity component obtained with the Saito model are closer to the results obtained numerically in [Gnanaskandan and Mahesh (2016)] who used the same method in conjunction with a

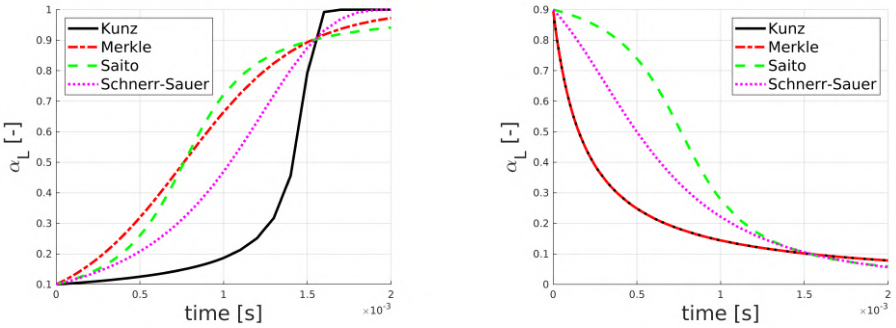

(a) Condensation process

(b) Vaporization process

Figure 3.13: Condensation and vaporization processes with analytical-based coefficients.

compressible-flow solver.

3.5 Results of normalized coefficients

We now discuss the results of the simulations performed considering the coefficients C_c and C_v calculated as described in Section 3.4. We emphasize that, since the Schnerr-Sauer model was taken as a reference to compute the time scales $T_{c,ref}$ and $T_{v,ref}$, results and observations concerning the Schnerr-Sauer simulation are the same reported in the previous Section 3.

Snapshots of the liquid-vapor fraction α_l obtained with the Kunz model with calculated coefficients are depicted in Figure 3.14. We observe a transitional regime with predominantly detached cavitation (Figure 3.14a–c). It is worth noting that, with the calculated coefficients, after the detachment of the vapor zones an attached cavity originates directly from the cylinder (Figure 3.14d) and extends downstream (Figure 3.14e,f) for a short period; however the simulation does not reproduce a stable attached cavity at the rear of the cylinder.

In Figure 3.15 we show snapshots of the liquid fraction obtained with the Merkle model, considering calculated coefficients (Table 3.9). Both detached (Figure 3.15a–c) and attached cavitation (Figure 3.15d–f) are visible. In this case, the vapor spots appear narrower than those observed in Figure 3.4 obtained with the standard coefficients, producing a different profile of the mean α_l along the centerline, as it will be shown in the following. Regions of attached cavities are still visible, albeit of smaller extension and for a shorter period, but generated from the cylinder itself, and extending downstream (Figure 3.15d–f); the shape of cavitation is very similar to that obtained with the Kunz model with calculated coefficients.

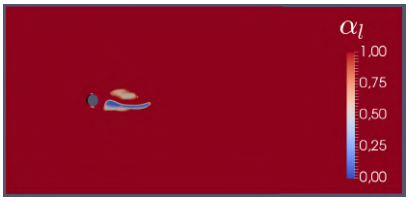

(**a**) $tD/U_\infty = 43$.

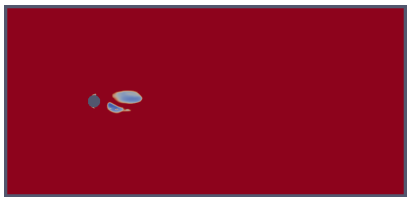

(**b**) $tD/U_\infty = 44$.

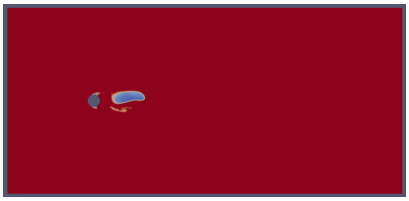

(**c**) $tD/U_\infty = 45$.

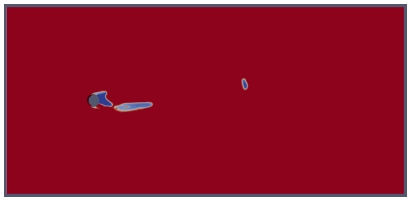

(**d**) $tD/U_\infty = 82$.

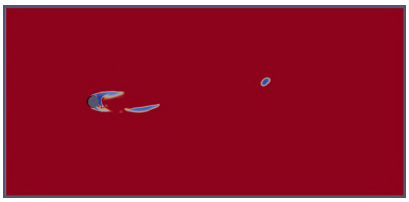

(**e**) $tD/U_\infty = 84$.

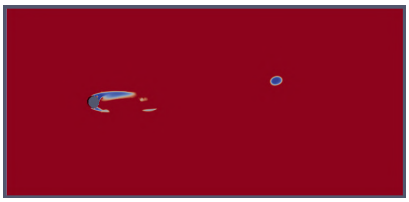

(**f**) $tD/U_\infty = 85$.

Figure 3.14: Contour plot of instantaneous liquid fraction, results obtained with Kunz model and considering analytical-based coefficients (Table 3.9).

Figure 3.16 shows snapshots of α_l from the simulation performed with Saito's model with the calculated coefficients, reported in Table 3.9.

The new coefficient setup makes the cavity dynamics of the Saito model similar to that observed with the other models, in particular with that of the Schnerr-Sauer one. Indeed, the cyclic regime disappears, and both detached and attached cavitation occur (see, respectively, Figures 3.16a–c and Figures 3.16d–f).

In Figure 3.17, the time-averaged liquid fraction α_l is depicted. We note that the behavior of the cavitation is similar for all models; the main difference concerning the standard-coefficients case is observed for the Saito model which, as expected, in this case, exhibits a more intense vapor phase.

Figure 3.18 shows the mean liquid fraction evaluated along the centerline, downstream of the cylinder. The models of Merkle and Kunz behave similarly to each other. Conversely, the models of Saito and Schnerr-Sauer produce more vapor fraction than the others. The difference is due to the cavitation regime reproduced by the models; in the case of Kunz and Merkle it is transitional with a strong prevalence of the detached component mainly

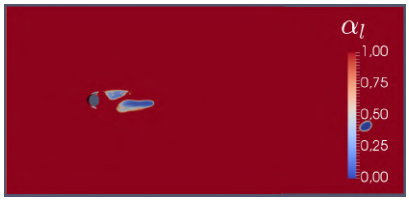

(**a**) $tD/U_\infty = 93$.

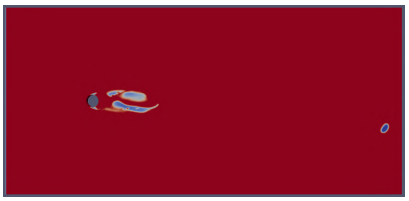

(**b**) $tD/U_\infty = 95$.

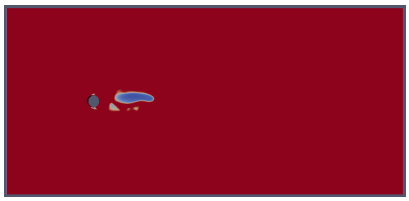

(**c**) $tD/U_\infty = 97$.

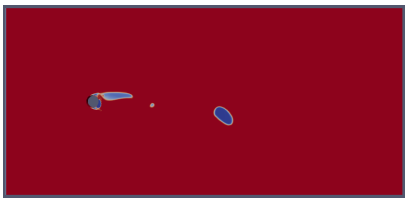

(**d**) $tD/U_\infty = 80$.

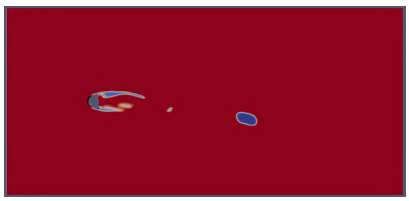

(**e**) $tD/U_\infty = 82$.

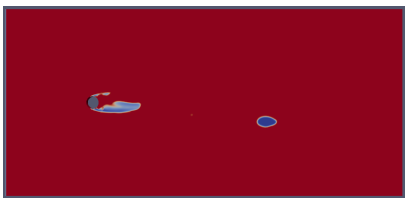

(**f**) $tD/U_\infty = 84$.

Figure 3.15: Contour plot of instantaneous liquid fraction, results obtained with Merkle model and considering analytical-based coefficients (Table 3.9).

distributed on the sides with respect to the centerline; the Saito and Schnerr-Sauer models produce a transitional regime but with a more stable cavity which occupies the central area at the rear of the cylinder and a higher percentage of mean vapor.

Figure 3.19 shows the variance of the stream-wise component of the velocity $\langle u'u' \rangle / U_\infty^2$. The figure shows that with the new coefficients, the Saito model tends to give results more similar to those of the other models. As observed in [Gnanaskandan and Mahesh (2016)], when cavitation moves from a cyclic regime to a transitional one, the peak of $\langle u'u' \rangle / U_\infty^2$ moves downstream, and their value increases, coherently with the cavitation regime observed. The variance has practically the same behavior for all models in the area immediately downstream of the cylinder and is characterized by a linear increase. For this quantity, we note that the Kunz model produces a peak a bit more downstream than the other models, although it behaves similarly to the Schnerr-Sauer model in the far field.

Figure 3.20 shows the spectra of the lift coefficients. All models exhibit a broad-band behavior, making the computation of the Strouhal number not

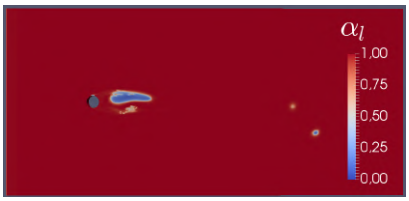

(**a**) $tD/U_\infty = 64$.

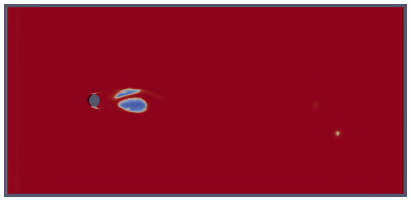

(**b**) $tD/U_\infty = 66$.

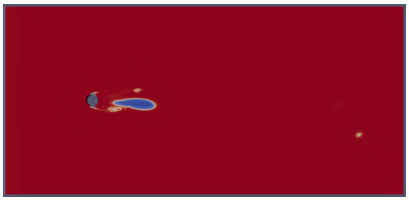

(**c**) $tD/U_\infty = 68$.

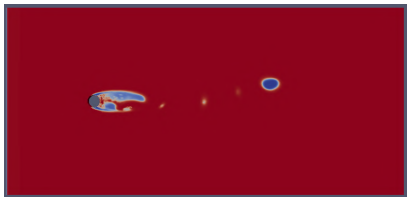

(**d**) $tD/U_\infty = 90$.

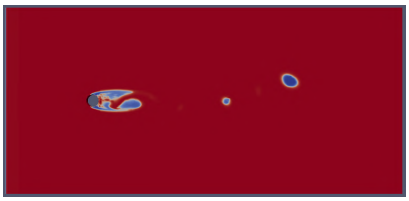

(**e**) $tD/U_\infty = 92$.

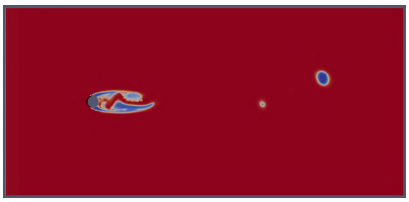

(**f**) $tD/U_\infty = 95$.

Figure 3.16: Contour plot of instantaneous liquid fraction, results obtained with Saito model and considering analytical-based coefficients (Table 3.9).

straightforward. The Schnerr-Sauer model has the main peak not coincident with those of the others, while all the other models have practically the same value for the vortex shedding frequency. The values observed are consistent with the literature, since the Strouhal number for the single-phase case is $St = 0.2$, and it decreases as the cavitation number decreases.

Figure 3.21 shows the mean pressure over the cylinder; the analytical evaluation of the coefficients leads to more similar values of pressure both in the upstream stagnation point and in the downstream region, where all models give pressure values in between the Schnerr-Sauer model and the literature value [Gnanaskandan and Mahesh (2016)]. Furthermore, in this case, we observe the presence of spots of the positive value of the mean σ_{loc}, for $\theta \in [80, 120]$; for this quantity as well, we note that the models with the coefficients calculated analytically have more consistent behavior.

For all simulations, the length of the attached cavity, the length of vortex formation, and the vortex shedding frequency were evaluated from the data shown, respectively, in Figures 3.18–3.20. The quantities are collected in Table 3.10.

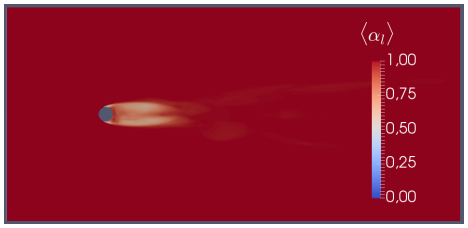

(**a**) Kunz model.

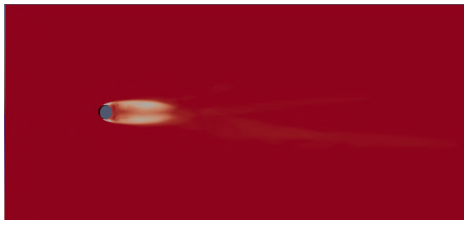

(**b**) Merkle model.

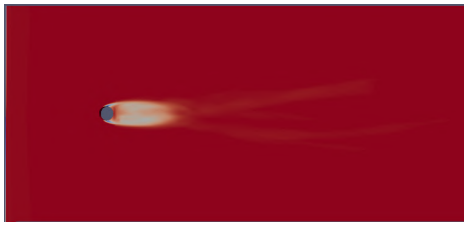

(**c**) Saito model.

(**d**) Schnerr-Sauer model.

Figure 3.17: Contour of time-averaged liquid fraction, results obtained considering analytical-based coefficients.

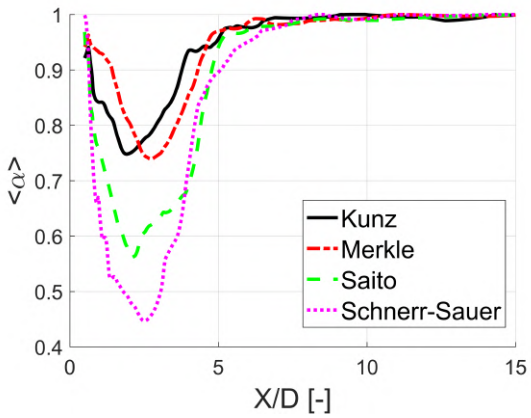

Figure 3.18: Mean liquid fraction downstream the cylinder along the centerline, results obtained considering analytical-based coefficients.

As a final analysis, to quantify the differences among the results given by the models before and after the computation of the coefficients, we calculate the variance between the results for the three quantities, and the values obtained are gathered in Table 3.11.

The variance of the length of vortex formation is a bit larger after the direct calculation of the coefficients. On the other hand, for the length of the attached cavity, and the mean vapor fraction downstream of the cylinder, it

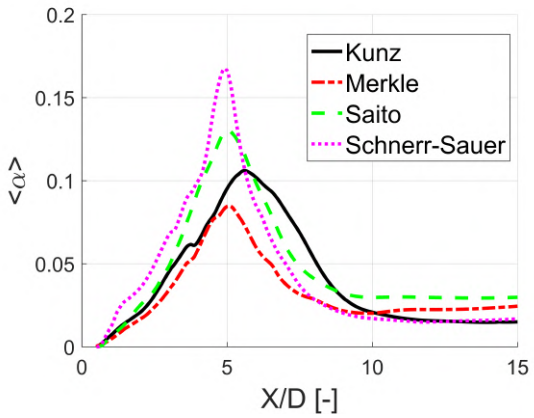

Figure 3.19: Variance of stream-wise velocity component downstream the cylinder along the centerline, with analytical-based coefficients.

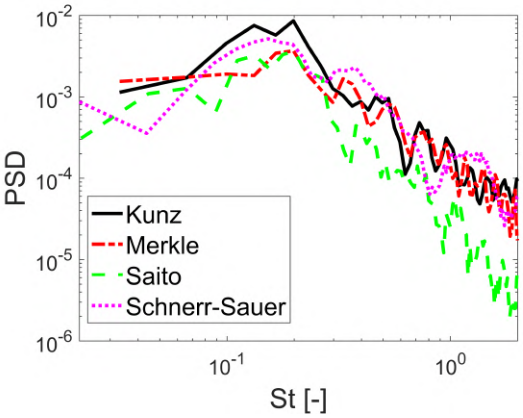

Figure 3.20: Lift coefficient spectrum with analytical-based coefficients.

can be observed that after computation of the coefficients, the models behave much more similarly to each other, as can be observed from the comparison between Figures 3.7 and 3.17. It is noted that the variance between the results decreases by almost 70% once the coefficients are calculated directly using the procedure suggested in the present paper. Moreover, we note that with the new coefficients all models exhibit a broad-band behavior for the spectra of the lift coefficient, and the vortex shedding frequency evaluated appears much more similar among the models, which leads to a variance that is one order of magnitude lower than that obtained for the standard coefficients.

The results shown above indicate that the analytical evaluation of the coefficients of the model improves the quality of the results. This is mostly evident in the Saito model. The Kunz and Merkle models behave very sim-

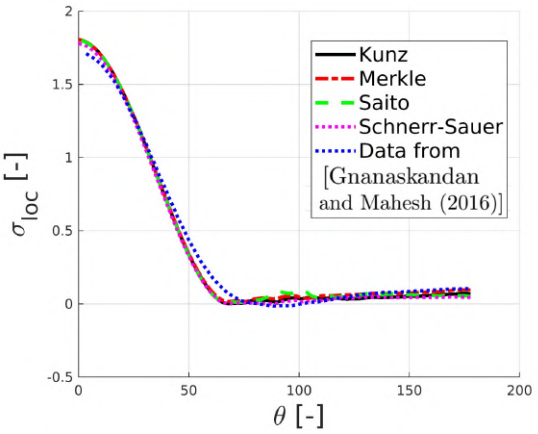

Figure 3.21: Mean pressure on the cylinder surface considering analytical-based coefficients.

Model	**Mean Length of Attached Cavity**	**Vortex Formation Length**	**Vortex Shedding Frequency**
Kunz	4.96 D	5.60 D	0.194
Merkle	4.66 D	5.07 D	0.195
Saito	5.10 D	5.01 D	0.195
Schnerr-Sauer	5.98 D	4.93 D	0.165

Table 3.10: Results of length of attached cavity, vortex formation length and non-dimensional vortex shedding frequency with analytical-based coefficients.

	Mean length of Attached Cavity	**Vortex Formation Length**	**Vortex Shedding Frequency**
Standard C_c, C_v	0.766	0.042	$1.64 * 10^{-3}$
Analytical-based C_c, C_v	0.241	0.069	$1.66 * 10^{-4}$

Table 3.11: Variances for the results of the length of the attached cavity, vortex formation length, and vortex shedding frequency for standard and analytical-based coefficients.

ilarly and exhibit differences from the Schnerr-Sauer model. This may be due to the derivative of α (see right panel of Figure 3.13) which changes dramatically from the Kunz and Merkle models to the Saito and Schnerr-Sauer models. Finally, we performed a grid-sensitivity test, considering a grid coarser than that discussed in the present Section. The analysis (herein

not described in detail) shows that the analytical evaluation of the coefficients provides some improvement in the results even in the presence of a coarse mesh, although better results are obtained with a good quality mesh.

3.6 Concluding Remarks

In this section, we proposed an analytical approach to calculate the coefficients of cavitation models, based on the reference time needed for vaporization/condensation processes, from a volume fraction α_0 to a value α_1, in an archetypal situation characterized by a constant pressure field and neglecting advective transport. This approach was then tested for four different models (Kunz, Merkle, Saito, and Schnerr-Sauer) considering the two-dimensional laminar flow around a circular cylinder. The simulations were performed earlier with standard literature coefficients and now with the new values calculated using this new approach. The results were analyzed and compared based on the consistency for the various models and concerning a literature case [Gnanaskandan and Mahesh (2016)] as regards various characteristics and physical quantities of the simulations; in particular, for each model, we first evaluated the cavitation regime reproduced and successively we calculated the mean pressure over the cylinder, the length of the attached cavity, the length of vortex formation and the vortex shedding frequency. It was noticed that, as a result of the analytical evaluation of the coefficients, for some models, there is a considerable improvement in the results regarding the cavitation regime and the reference quantities above reported, in particular for the Saito model; specifically the Saito model used with the standard coefficients was found to predict a cyclic regime instead of the transitional one reproduced by the other models; the same model, with the analytically calculated coefficients predicts a transitional regime with a more stable attached cavity, likewise the Schnerr-Sauer model, which in our study has been taken as a reference for the evaluation of the reference times for condensation/vaporization. Regarding the Kunz and Merkle models, it was found that after the analytical evaluation of the coefficients the two models behave similarly to each other, even if they behave differently from the Schnerr-Sauer model, in that they are not able to develop the stable cavity attached to the rear of the cylinder. Specifically, an attached cavity tries to form in contact with the cylinder but it rapidly disappears. On the other hand, the use of standard values of the coefficients leads to the development of a cavitation region at the rear of the cylinder, from the vapor present in the vortices and collapsing shortly after. Overall, this study shows that the use of analytically based coefficients significantly improves the performance of some models, in particular if the regime previously obtained was different, while for others the improvement was not so evident; this may be due to different reasons: among them, the range of values for the volume fraction

used to calculate the coefficients, the fact that the condensation and evaporation time scales are assumed to be the same, and, finally, the fact that the reference model herein used (Schnerr-Sauer model) is already a simplified model derived from the more complete and physical-based Rayleigh-Plesset equation.

Chapter 4

2D Cavitating vortex

As already pointed out in the Introduction (Chapter 1), the study of the tip vortex released by the blades of the propeller, is gaining increasing interest, especially if it's associated with cavitating conditions; indeed, the tip vortex cavitation has been often identified as the main source of noise from the ship propeller, that is a major problem concerning units, like research and passenger ships who are expected to be classified as 'silience shpis' according to the rules of Classification Societies [www.vesselfinder.com]. Here we focus on the dynamics of an isolated cavitating vortex as the one presented in the work of Bosschers [Bosschers (2018)].

4.1 Analytical results

In this chapter we use cylindrical coordinates (r, θ, z) with the vortex axis coincident with the axes z, more suited than the Cartesian ones for the present problem; in the two-dimensional case the coordinates reduced to (r, θ). In [Bosschers (2018)] the author studied the dynamics of cavitating vortexes considering the hypothesis of incompressible and laminar liquid flow, and different vortex profiles were adopted in their analysis. To identify the dynamics and the homogeneous oscillation mode the author used the incompressible Navier-Stokes equations in polar coordinates

$$\begin{cases} \frac{1}{r}\frac{\partial}{\partial r}(ur) = 0, \\ \frac{\partial u}{\partial t} + u\frac{\partial u}{\partial r} - \frac{v^2}{r} = -\frac{1}{\rho}\frac{\partial p}{\partial r} + \frac{\mu}{\rho}\frac{\partial}{\partial r}\left[\frac{1}{r}\frac{\partial (ur)}{\partial r}\right], \\ \frac{\partial v}{\partial t} + u\frac{\partial v}{\partial r} - \frac{uv}{r} = \frac{\mu}{\rho}\frac{\partial}{\partial r}\left[\frac{1}{r}\frac{\partial (vr)}{\partial r}\right] \end{cases} \tag{4.1}$$

The interactions between the gas and the liquid is modeled through the boundary conditions

$$\begin{cases} u_c = \frac{dr_c}{dt} = \dot{r}_c, \\ p_c - 2\mu\left(\frac{\partial u}{\partial r}\right)_c = p_v, \\ \left(\frac{\partial v}{\partial r}\right)_c - \frac{v_c}{r_c} = 0 \end{cases} \tag{4.2}$$

The theory presented by Bosschers reproduces a cavitating vortex and does not consider mass transfer between the liquid and the vapor or any change in the vapor pressure that is considered equal to p_v.
To identify the cavity characteristics, different velocity profiles for the vortex can be evaluated analytically; here we consider the vortex velocity as expressed by the Burnham-Hallock [Burnham and Hallock (1982)] formulation:

$$v_\theta(r) = \frac{\Gamma_\infty r}{2\pi\left(r_v^2 + r^2\right)} \tag{4.3}$$

where Γ_∞ is the far-field circulation of the vortex, r_v is the viscous radius while r is the distance from the center of the vortex. Considering the vortex and the cavity in equilibrium condition, we can identify the radius $\bar{r}_c := r_{p=p_v}$ which is the radius at which the fluid dynamic pressure is equal to the vapor pressure; using equation (4.2), it can be evaluated as:

$$\overline{r_c} = \sqrt{\frac{1}{\frac{(p_{ref}-p_v)8\pi^2}{\rho\Gamma_\infty^2} + \left(\frac{1}{r_v^2+r_{ref}^2}\right)} - r_v^2} \tag{4.4}$$

The natural frequency associated with the oscillation of the cavity can be evaluated as:

$$\omega = \frac{1}{\overline{r_c}}\sqrt{\frac{p_{ref}-p_v}{\frac{1}{2}\rho\left[1+\left(\frac{r_v}{\overline{r_c}}\right)^2\right] ln\left(\frac{r_{ref}}{\overline{r_c}}\right)}} \tag{4.5}$$

4.2 Numerical settings

The present section aims to reproduce the dynamics of the two-dimensional cavitating vortex using numerical approaches commonly used in engineering applications. As for the previous section, we use the opensource software OpenFOAM, considering the interPhaseChangeFoam solver. This solver adopts the hypothesis of two incompressible and immiscible fluids with phase-change and the PIMPLE algorithm to solve the Navier-Stokes equations and the volume fraction transport equation; the model used in these simulations for the cavitation vaporization-condensation processes is that of Schnerr-Sauer.

In the simulations, we consider a circular domain coaxial with the axis of the vortex. The grid adopted is unstructured but composed of structured blocks, in particular, the blockMesh utility was adopted to build a (mostly) axial-symmetrical grid.
The mesh is made of four different concentric regions, from the center to the external boundary the grid is built as follows: Internal region, the intermediate region, the interface region, and the external region. An Internal Region (depicted in Figure 4.1a) covers the vortex core with Cartesian cells;

an Interface Region (depicted in Figures 4.1b and 4.1c) is accurately refined in order to capture the small-amplitude oscillations of the cavity interface; an Intermediate and External Regions (depicted in Figures 4.1b and 4.1d), are opportunely stretched along the radial direction, in order to optimize the whole grid point distribution.

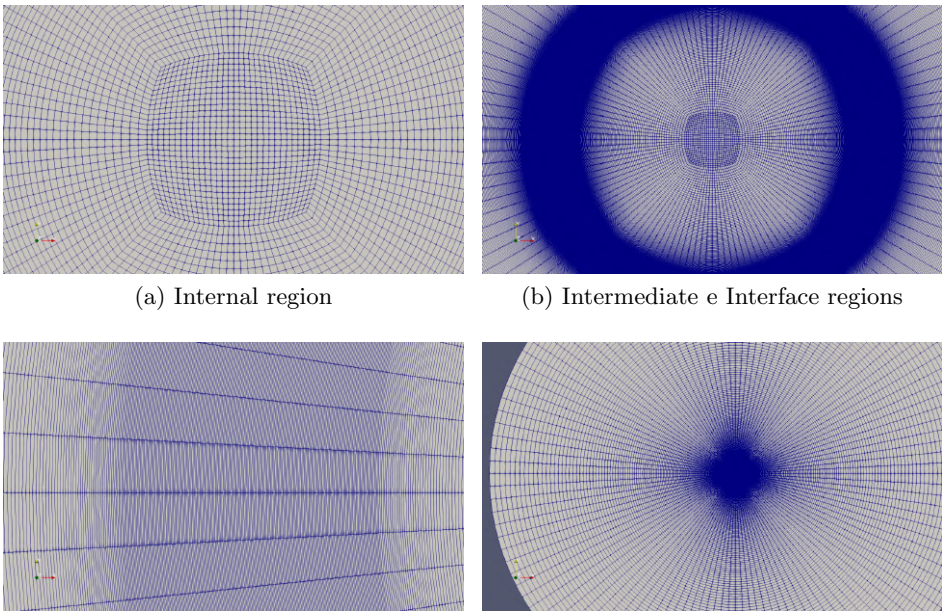

(a) Internal region

(b) Intermediate e Interface regions

(c) Interface region

(d) External region

Figure 4.1: Plot of the evolution of the cavity with the previous setting.

The dimension of the regions used to build the mesh and the stretching adopted are collected in Table 4.1 To initialize the field we started consid-

region	**characteristic**	**value**	
Internal region	Length dimension	0.01	(m)
Intermediate region	Maximum radius	0.015	(m)
	Stretching	0.1	$(-)$
Interface region	Maximum radius	0.02	(m)
External region	Maximum radius	1	(m)
	Stretching	800	$(-)$

Table 4.1: Mesh dimension and characteristics.

ering a single phase (liquid) with homogeneous field for velocity, pressure, and volume fraction. In particular, the steps adopted are the following:

- we impose the velocity field on the domain according to the equation (4.3),

- we let the solver adjusting the pressure field with a short simulation of 3 iterations without considering phase change,
- starting from the field obtained in step 2, where the flow pressure falls below the vapor pressure ($p <= p_v$) we set $\alpha_v = 0.99$ and $p = p_v$:

$$\alpha_{v,new} = 0.99 \quad if \quad p <= p_v \tag{4.6}$$

$$p_{new} = p_v \quad if \quad p <= p_v \tag{4.7}$$

As boundary conditions on the far field, we use a constant value for the pressure and a zero gradient for the velocity and the volume fraction fields. Initially, a zero gradient condition was tested also for the pressure field, but with this condition, the simulation resulted unstable. The details of the simulation settings are collected in Table 4.2. Note that we consider an inviscid flow.

Property	**Symbol**	**Value**	
Vortex circulation	Γ_∞	1	(m^2/s)
Viscous radius	r_v	0.01	(m)
Reference pressure	p_{ref}	30000	(kg/ms^2)
Liquid density	ρ_l	1000	(kg/m^3)
Liquid viscosity	ν_l	0	(m^2/s)
Vapor density	ρ_v	0.02308	(kg/m^3)
Vapor viscosity	ν_v	0	(m^2/s)
Vapor pressure	p_v	2300	(Kg/ms^2)
Bubble density	n	$1.6 * 10^{13}$	$(1/m^3)$
Nucleus radius	d_{Nuc}	$2 * 10^{-6}$	(m)
Condensation coefficient	C_c	1	
Vaporization coefficient	C_v	1	

Table 4.2: Fluid, flow and simulation properties.

4.3 Results

The first test to evaluate the the solver's accuracy was carried out in absence of forcing external pressure, and we monitored the time evolution of the radius and the total mass of the phases in the domain. We considered the case where the pressure at the boundary is equal to the original value $p = 30000Pa$

The evolution of the radius for the cavitating flow, depicted in Figure 4.2a, shows that the simulation computes correctly the period of the oscillation. This oscillatory motion has to be associated with the imposed initial field that, does not match exactly the equilibrium condition. Indeed, the Figure shows a small amplitude oscillation oscillation with an amplitude of

$\approx 4 * 10^{-5}(m)$, and a small shift of radius during the simulation indicating the presence of the initial non-equilibrium condition. Also, check on the conservation properties of the solver was carried out considering the mass flow rate in the far field and the derivative of the mass over the entire domain, as depicted in Figure 4.2b. We can see that they have the same behavior, also if there is a peak during the first iterations, that confirm the fact that the initial condition, although not perfect, is good for the simulation and that the solver has good conservation properties.

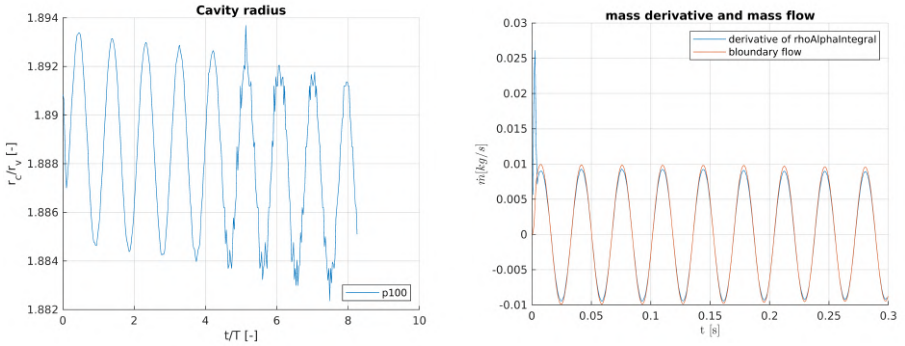

(**a**) Radius evolution

(**b**) Mass flow

Figure 4.2: Results of the simulation without pressure variation.

To simulate the oscillation of the cavity, after the initialization of the simulation with the reference pressure, it was imposed on all the far-field boundaries as the 99% of its initial value, which means that the value was set equal to $p_{ref} = 29700Pa$ to start from a non-equilibrium initial field.

The first test we carried out was aimed to identify and study the effect of the mesh on the quality of the results of the oscillation of the cavity; we considered three different meshes with the same dimensions and stretching factor reported in Table 4.1, and changing the number of radial and tangential cells; also, each mesh has twice as many cells in each direction compared with the previous coarse one. Table 4.3 reports the number of cells used for each mesh.

Characteristic	**Coarse**	**Middle**	**Fine**
Radial cells Intermediate region	50	100	200
Radial cells interface region	100	200	400
Radial cells external region	150	300	600
Tangential cells	60	120	240

Table 4.3: Characteristics of computational grids.

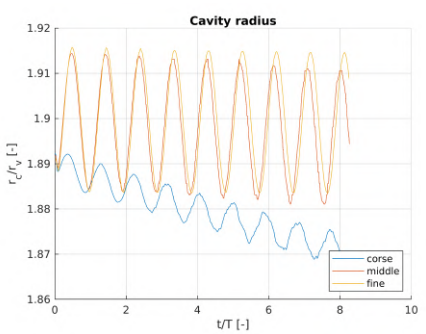

(a) Radius

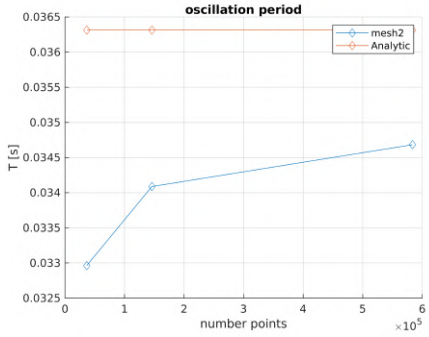

(b) Oscillation period

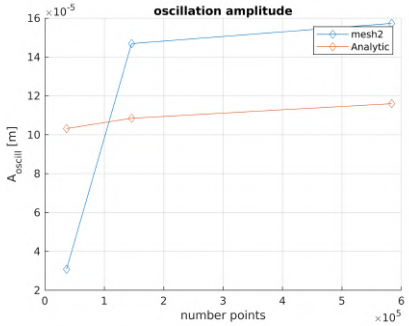

(c) Oscillation amplitude

Figure 4.3: Results of the two-dimensional cavitating vortexes for the parametric study on the mesh refinement.

The time evolution of the radius id depicted in Figure 4.3a for the computational grids employed.

We observe that the coarsest mesh is not fine enough to simulate correctly the evolution of the cavity, since the amplitude of the radius is quite smaller than those obtained with finer meshes. It is also worth noting that the average radius during the simulation with the coarsest mesh decreases, showing that the simulation does not conserve the mass of the cavity in time. Increasing the grid refinement, this undesirable effect is less and less present. In Figure 4.3a this effect is highlighted by comparing the data obtained with increasing mesh size.

The analysis of the oscillation periods (Figure 4.3a), show that increasing the grid size reduces the error, from the 10% of the coarsest mesh to less than 5% for our finer mesh. The simulation with the coarse mesh underestimates the amplitude of the radius, while the intermediate and the finest meshes overestimate the oscillation amplitude by about the same value roughly equal to $4 * 10^{-5}[m]$. This error is that of the oscillation in equilib-

rium consitions, as visible in Figure 4.2a; so this small contribution can be related to the mentioned problem with the initial condition.
The mesh herein employed share the weakness to be quite coarser in the tangential direction with respect to the radial direction. The mesh that we will use in the next test has the same radial discretization of the intermediate mesh and a tangential discretization finer than the finer mesh. The cells discretization used in the new mesh is reported in Table 4.4.

Characteristic	**Value**
Radial cells Intermediate region	100
Radial cells interface region	200
Radial cells external region	300
Tangential cells	400

Table 4.4: Characteristics of standard mesh.

The second test was carried out to evaluate the sensitivity of the results on the time step used in the simulations; the time steps adopted are reported in Table 4.5.

Tested value
$dt = 1 * 10^{-5}$
$dt = 2 * 10^{-5}$
$dt = 3 * 10^{-5}$
$dt = 4 * 10^{-5}$
$dt = 1 * 10^{-4}$

Table 4.5: Time steps employed in the simulations the free oscillation of the cavity.

The time evolution of the radius, the period and the amplitude of the oscillation are depicted in Figure 4.4. We observe that the time step of the simulation affects the predicted oscillation period, since it varies from case to case, with an error within 10% when compared to the analytical value. The oscillation amplitude is less sensitive to the time step, and, also in this case, it is about $4 - 5 * 10^{-5}[m]$ higher than the analytical expectation, due to the initialization problem already mentioned.

The third test regards the comparison of the results obtained changing the value of the coefficients of the cavitation model C_c and C_v, as reported in Table 4.6.

The results of this test are collected in Figure 4.5
The simulation with the coefficients set equal to zero $C_c = C_v = 0$ is the only one without any change in the cavity radius, because this setting

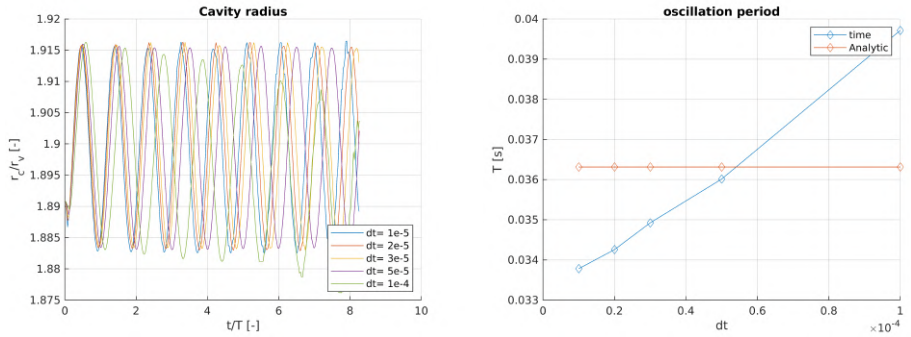

(a) Radius

(b) Oscillation period

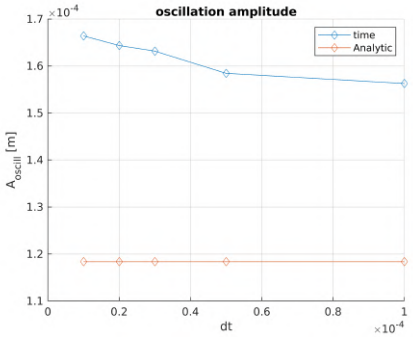

(c) Oscillation amplitude

Figure 4.4: Results of the time evolution of the two-dimensional cavitating vortex under variation of the time step.

doesn't allow the phase change and the radius remains constant over a time window period that ends with a numerical instability of the simulation. This happens because setting the coefficients to zero prevent the cavity from expanding, but since the forcing pressure remains, and since the solver is implicit in the pressure, the simulation manages to continue until some symmetry is maintained, but small numerical variations after a while lead to the simulation instability. On the other hand, the two simulations with the higher values $C_c = C_v = 30, 100$ are unstable and the simulations

cannot run neither for a complete single cavity oscillation and are not visible in the graph 4.5a. For all the other coefficient values we can notice that the radius, depicted in Figure 4.5a does not change much from case to case with small differences in the amplitude (Figure 4.5b). Also, the error in the period of the oscillation (Figure 4.5c) remains within the 10%

Finally, in all simulatoins we note the drifting of the mean radius in time (Figure 4.5c and Figure 4.5d) with larger values in presence of higher value of coefficients.

Tested values
$C_c = C_v = 0$
$C_c = C_v = 0.1$
$C_c = C_v = 0.3$
$C_c = C_v = 1$
$C_c = C_v = 3$
$C_c = C_v = 10$
$C_c = C_v = 30$
$C_c = C_v = 100$

Table 4.6: Vaporization and condensation coefficients considered in the simulations.

FInally, we noticed that increasing the value of the coefficients may lead to small instabilities and damping of the mean radius. This effect of numerical damping is visible also if the simulation is stable with results reasonably accurate.

4.4 Cartesian mesh

So far, we analyzed the dynamics of an isolated vortex using an axial-symmetrical mesh characterized by a refinement on the interfacial region. However, for common engineering applications, this type of grid is not feasible, due to both the number of grid points needed and for the specific cylindrical shape. This is the reason why the previous mesh is not suited for the analysis of industrial processes, where geometry complexities are the rule and computational cells are often of hexahedral or polyedral shape. So we decided to test the simulation of the two-dimensional homogeneous pulsating cavity vortex using a Cartesian mesh; in particular, we used a circular mesh for the far-field vortex and a Cartesian core region that contains completely the cavity. An example of mesh is depicted in Figure 4.6. Different meshes were considered. Vortex dynamic is analyzed and results are compared with previous data, obtained for the axial-symmetric grid. The parameters for the grids herein adopted are collected in Table 4.7. The different levels of

Characteristic	Symbol	Value	
Radius of the domain	R_{max}	1	(m)
Length of the Cartesian core	l_{core}	0.05	(m)
Stretching		50	

Table 4.7: Characteristics of the Cartesian meshes.

refinement of the mesh are controlled by the number of cells contained in

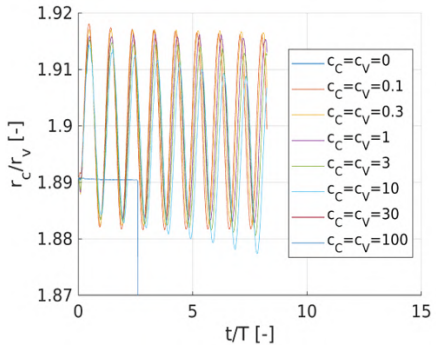

(a) Radius

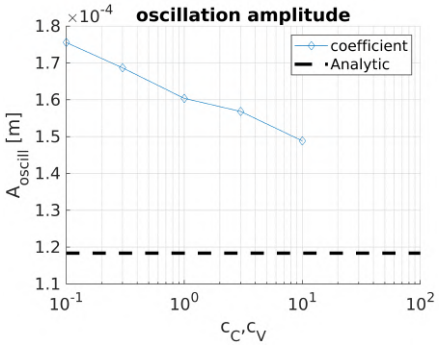

(b) Oscillation amplitude

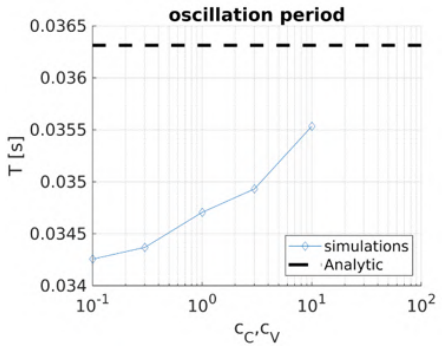

(c) Oscillation period

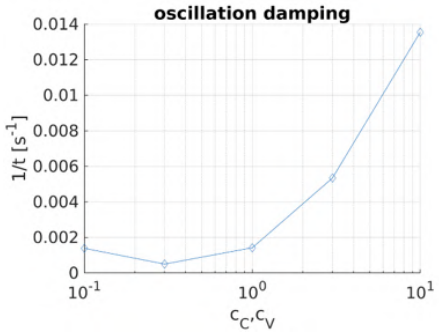

(d) Oscillation damping

Figure 4.5: Results of the two-dimensional cavitating vortex for the parametric study on the coefficients for the cavitation model.

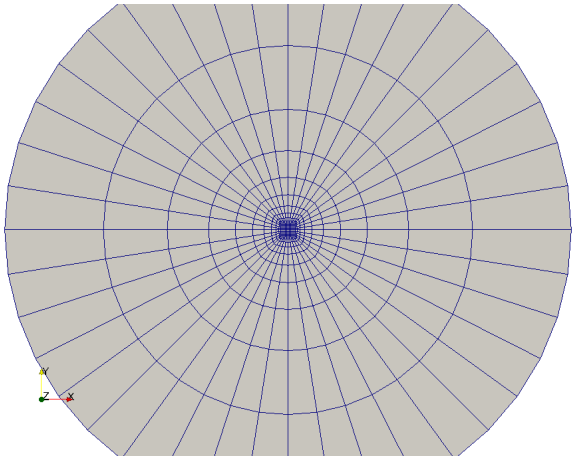

Figure 4.6: Geometry of coarser mesh tested to simulate the vortex.

the Cartesian core region. Table 4.8 summarizes the levels of refinement

considered.

Mesh	n_{cell} **along** l_{core}
Mesh 0	10
Mesh 1	20
Mesh 2	45
Mesh 3	100
Mesh 4	200
Mesh 5	450
Mesh 6	1000

Table 4.8: Number of cells along the length of the core region for the different levels of refinement.

To be noted that the different levels of refinement of the internal Cartesian region affects the smoothness of the circular cavity. A picture showing the initial shape of the cavity is reported in Figure 4.7, concerning Mesh0, Mesh1, Mesh2, Mesh3, and Mesh4.

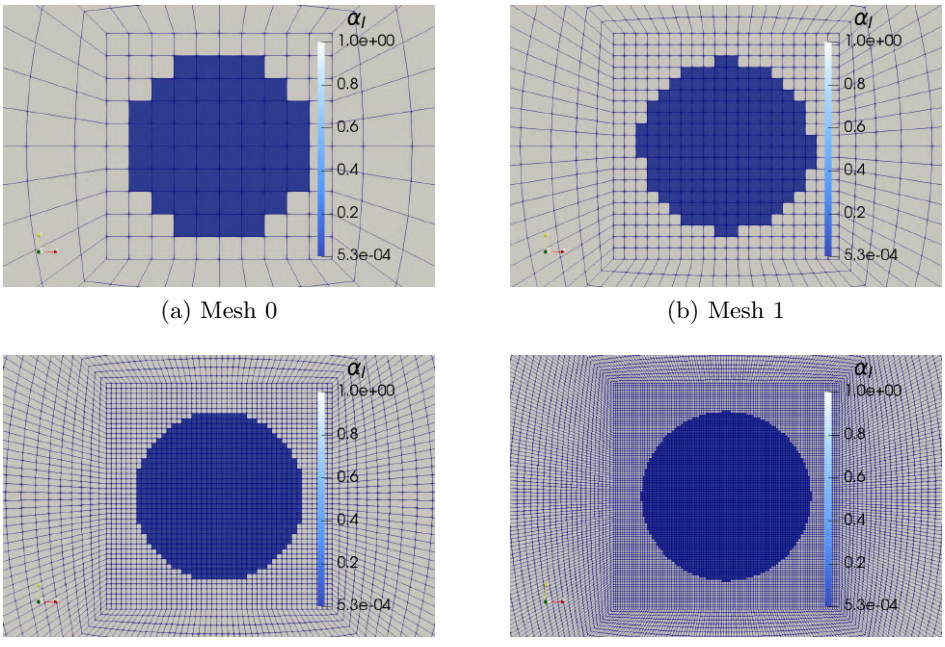

(a) Mesh 0 (b) Mesh 1

(c) Mesh 2 (d) Mesh 3

Figure 4.7: Initial liquid volume fraction field for the cavity detail for some square grids.

The simulation with the coarsest mesh, as depicted in Figure 4.8, shows the oscillatory pattern of the cavity together with (4.8a-4.8e) a constant

reduction of the cavity region (Figures 4.8e-4.8h). The mean radius decreases due to the insufficient number of cells used to simulate the cavity in conjunction with a mesh geometry not suited for axial-symmetric problems. This is particurarly true when comparing the results with the almost perfect oscillatory motion previously observed in the simulation with the axial-symmetrical and refined mesh.

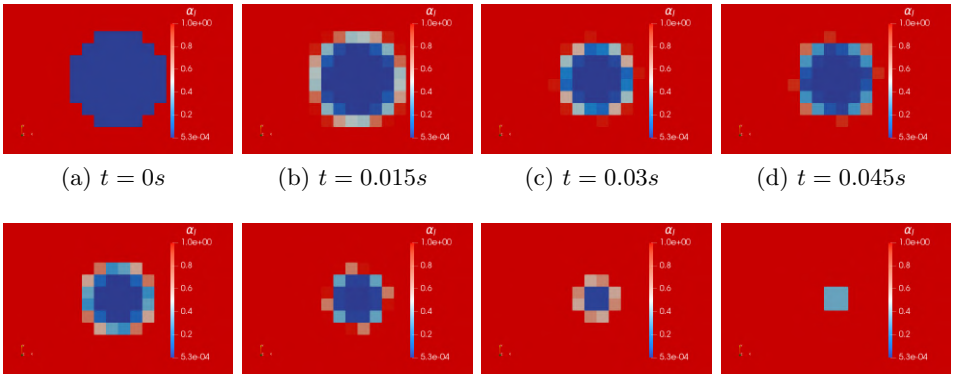

(a) $t = 0s$ (b) $t = 0.015s$ (c) $t = 0.03s$ (d) $t = 0.045s$

(e) $t = 0.060s$ (f) $t = 0.120s$ (g) $t = 0.180s$ (h) $t = 0.240s$

Figure 4.8: Dynamicc of the vapor cavity for the simulation Mesh0.

The simulation Mesh1, depicted in Figures 4.9 shows the same behavior of the previous simulation Mesh0 but with a less relevant collapse of the cavity.
The first period of oscillation, is hardly visible in the Figures (4.9a-4.9e) while the reduction of the radius is visible in the Figures (4.9e-4.8h)

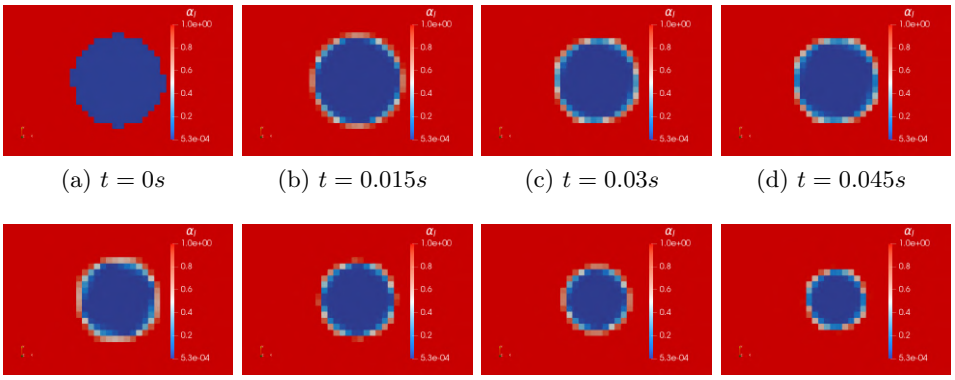

(a) $t = 0s$ (b) $t = 0.015s$ (c) $t = 0.03s$ (d) $t = 0.045s$

(e) $t = 0.060s$ (f) $t = 0.120s$ (g) $t = 0.180s$ (h) $t = 0.240s$

Figure 4.9: Dynamic of the vapor cavity for the simulation Mesh1.

The simulation Mesh2, as shown in Figure 4.10 gives results in good agreement with the analytic ones, depicted in Figure 4.10a-4.10e, and the

reduction of the mean radius is not clearly visible after four oscillations, as shown in Figures 4.10e-4.10h; However, letting the simulation run, some spurious values of velocity are visible at the interface (see Figure 4.10h); later on, these spurious values appear also inside the cavity and lead to the simulation instability.

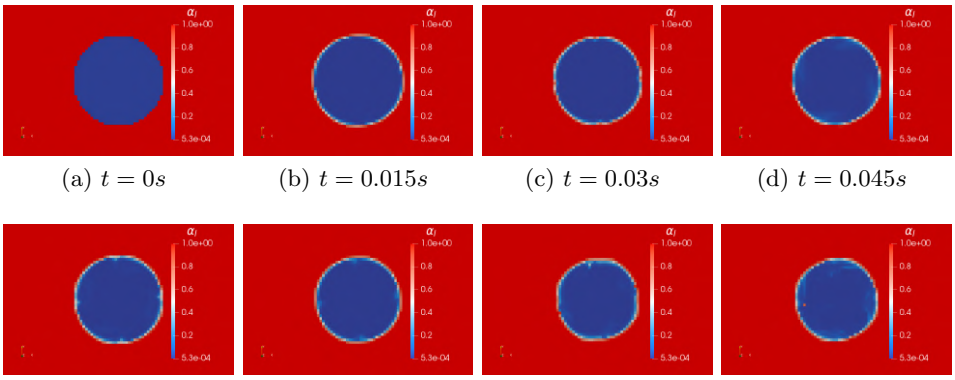

(a) $t = 0s$ (b) $t = 0.015s$ (c) $t = 0.03s$ (d) $t = 0.045s$

(e) $t = 0.060s$ (f) $t = 0.120s$ (g) $t = 0.180s$ (h) $t = 0.240s$

Figure 4.10: Dynamics of the vapor cavity for the simulation Mesh2.

The simulation Mesh3 is in a good agreement with reference data for the first oscillatory cycle, however spurious numerical noise develops within the cavity (Figures 4.11a-4.11e), leading to an irregular shape cavity after only four oscillations, as depicted in Figure 4.11h.

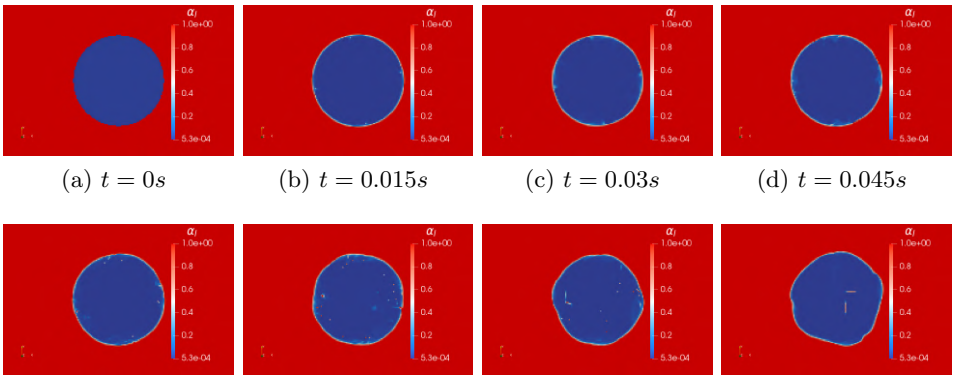

(a) $t = 0s$ (b) $t = 0.015s$ (c) $t = 0.03s$ (d) $t = 0.045s$

(e) $t = 0.060s$ (f) $t = 0.120s$ (g) $t = 0.180s$ (h) $t = 0.240s$

Figure 4.11: Dynamics of the vapor cavity for the simulation Mesh3.

Increasing the number of cells improves the accuracy of the results during the first oscillation of the cavity (Figures 4.12a-4.12e); However, the symmetrical shape is missed soon, as reported in Figures 4.12e-4.12h

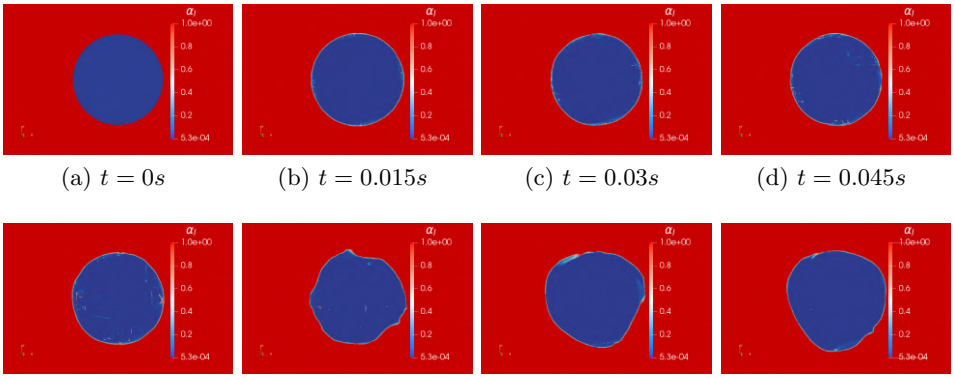

(a) $t = 0s$ (b) $t = 0.015s$ (c) $t = 0.03s$ (d) $t = 0.045s$

(e) $t = 0.060s$ (f) $t = 0.120s$ (g) $t = 0.180s$ (h) $t = 0.240s$

Figure 4.12: Dynamics of the vapor cavity for the simulation Mesh4.

To study the dynamics of the cavity we analyzed also the evolution of the radius of the cavity in time (Figure 4.13a). We can identify two different unphysical issues related to the mesh shape. In particular, the damping of the radius during the oscillation of the cavity, and the numerical instability represented by the deformation of the liquid-vapor interface from the circular shape to an irregular one.
The reduction of the area of the mean cavity (Figure 4.13b) decreases with the increasing number of cells of the mesh. On the other hand, increasing the number of cells brings the simulation to have some numerical instability and modify the shape of the interface toward a non-axial-symmetrical shape; in this case, the use of higher order numerical schemes may be helpful to increase the quality of the results.

4.5 Concluding Remarks

In this Chapter, we reproduced numerically and analyzed the case of a two-dimensional cavitating vortex, and the results were compared with the analytical solution available in literature [Bosschers (2018)]. In particular, the dynamics simulated is the homogeneous pulsating cavity, where the oscillatory motion was forced with a pressure jump at the boundary. Different numerical configurations were adopted and compared; in particular, different levels of mesh refinement, time steps, and coefficients for the cavitation model were adopted using a grid mesh properly designed for such class of simulations; later on a Cartesian grid mesh was tested to better represent the typical mesh adopted in engineering applications.
Results obtained with the axial-symmetric mesh pointed out that a too-coarse mesh produces cavity oscillations with a reduced amplitude and a numerical damping; the coefficients of the cavitation model seemed to have

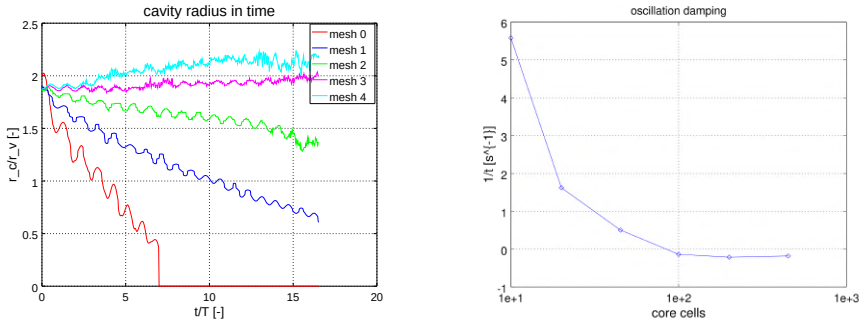

(a) Average radius (b) Radius damping

Figure 4.13: Dynamic of the mean average radius and damping the simulation with square mesh.

no particular influence on the reproduction of the correct dynamics, unless they are too high; in this latter case, they lead to numerical damping and instability. During the analysis of the Cartesian meshes different refinement types were adopted for the same numerical setting. The use of coarse meshes leads to a damping of the radius in time; this effect decreases with the refinement of the grid. However, highly-refined meshes let to numerical instability and unphysical oscillations of the cavity interface.

Chapter 5

3D Cavitating vortex

In this chapter we present a study on the dynamics of a three-dimensional vortex. First, the pulsating vortex is reproduced, which differs from the 2D case as there is now an axial velocity. Then, following the work of Bosschers, first oscillating modes are considered and we compare the results with the analytical solution. The tangential velocity of the 3D vortex is the one described by the Burnham-Hallock formula (eq. (4.3)), as in the 2D case.

5.1 Homogeneous pulsating mode

The first case analysed is the homogeneous vortex as in the simulations of the previous Section. After the initialization of the vortex with the imposition of the vapor phase in the core of the vortex, (i.e. where the vortex pressure given by the analytical single-phase vortex drops below the vapor pressure), three different simulations were carried out. The first simulation is relative to the cavity without variation of reference pressure and phase change; the second simulation is for the vortex without variation in the far-field pressure but allowing the phase change; in this case the two coefficients of the Schnerr-Sauer model are set to $C_c = C_v = 1$; the third simulation is the case with mass-transfer and with a change of pressure in the far-field, with a value that is the 99% of the original value. The value of the far field pressure and the coefficients are collected in Table 5.1 The dynamics of the three simulations

simulation	**far-field pressure**	**cavitation coefficients**
Case 1	$p_{ref} = 30000Pa$	$C_c = C_v = 0$
Case 2	$p_{ref} = 30000Pa$	$C_c = C_v = 1$
Case 3	$p_{ref} = 29700Pa$	$C_c = C_v = 1$

Table 5.1: Setting for the simulation of the 3D homogeneous vortex.

are depicted in Figure 5.1. As expected, different behaviors are observed; in particular, switching-off the phase-change and without varying the reference

pressure, the radius is stable in time. On the other hand, allowing change of phase and imposing a jump in pressure at the external boundary, excite the vortex oscillation. The oscillation period is the same observed in the previous two-dimensional cases and, likewise, we noticed that in the first time steps there are a cavity compression, even if the external pressure should produce an expansions. This phenomenon, induced by a numerical slight unbalance of the initial conditions, induces an initial oscillation also in the case without any pressure variation, that should be stationary.
Case 2, characterized by mass transfer but without the forcing pressure variation shows an oscillation with an amplitude equal to the one already identified in the two-dimensional simulations.

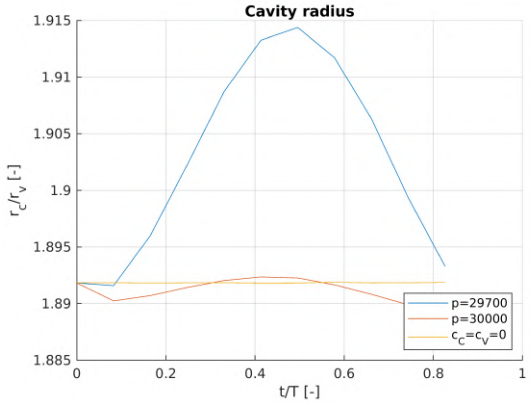

Figure 5.1: Radius dynamics for the three dimensional homogeneous simulations.

5.2 Helicoidal natural mode

As reported in Bosschers, natural modes can be excited by considering an initial condition for the cavity shape so as to be non-symmetrical in the tangential direction and non-homogeneous in the axial direction. The cavity radius herein considered changes along the axial direction, thus, to monitor its own evolution correctly we have placed several probes at different locations, both in the axial direction and in the radial direction, considering a single value for the tangential angle θ, since the problem is axial-symmetric. A draft of the sets of probes considered is depicted in Figure 5.2.

5.2.1 Analytic vortex

Every natural mode can be described by two parameters. The first one represents the length of the oscillation in the axial direction namely the

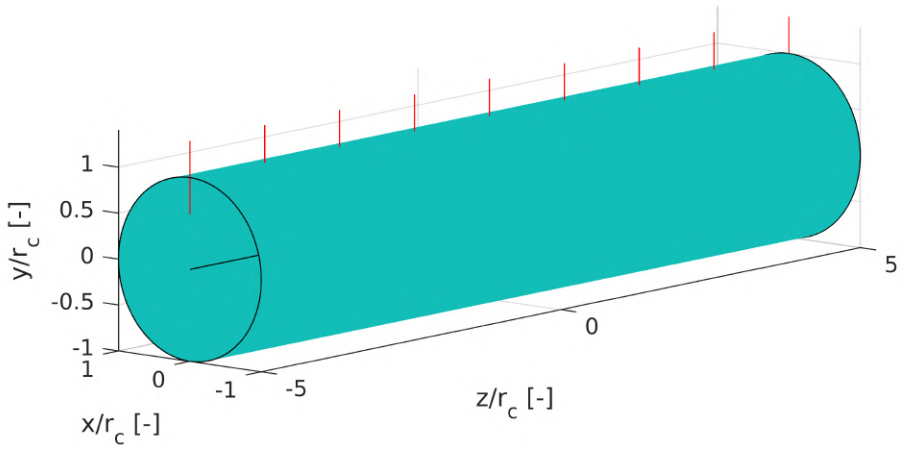

Figure 5.2: Location of the probes to evaluate the cavity interface, for the three-dimensional natural helicoidal modes of the vortex.

axial wavenumber k_z that in a domain with length Δz is expressed as:

$$k_z = \frac{n_z 2\pi}{\Delta z} \tag{5.1}$$

with n_z the number of oscillations in the axial direction. The second parameter is the number of oscillations in the tangential direction n_θ, and this value has to be an integer. Once the mode is defined by the pair n_z , n_θ, the cavity dynamics is determined. In particular, the distance of the interface from the vortex axes for each point (θ, z, t) is described by:

$$r_c(\theta, z, t) = r_{c,0} + \eta_0 e^{(k_z z + n_\theta \theta + \omega t)} \tag{5.2}$$

A sketch of the natural modes with $n_z, n_\theta \subset [0, 1, 2]$ is depicted in the Figure 5.3. Each natural mode of the vortex is characterized by its own frequency.
We note that the tangential perturbation (i.e. when considering $n_\theta > 0$) provides for two natural frequencies, related to two different directions of propagation of the perturbation. The analytical formulation of the frequencies was found by Bosschers[Bosschers (2018)]:

$$\omega^{\pm}(k_z, n_\theta) = W_c k_z + \Omega n_\theta \pm \frac{W_\infty}{r_c}\sqrt{K_\sigma}\sqrt{\frac{-k_r r_c H_{n_\theta}^{(1)'}(k_r r_c)}{H_{n_\theta}^{(1)}} T_\omega} \tag{5.3}$$

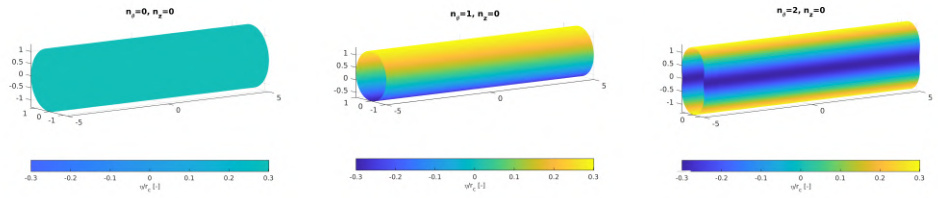

(a) Draft of the natural mode $n_z = 0, n_\theta = 0$ (b) Draft of the natural mode $n_z = 0, n_\theta = 1$ (c) Draft of the natural mode $n_z = 0, n_\theta = 2$

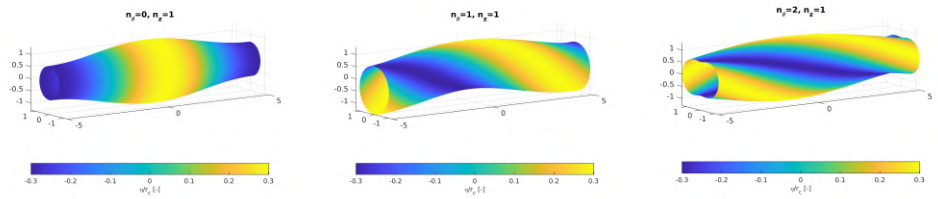

(d) Draft of the natural mode $n_z = 1, n_\theta = 0$ (e) Draft of the natural mode $n_z = 1, n_\theta = 1$ (f) Draft of the natural mode $n_z = 1, n_\theta = 2$

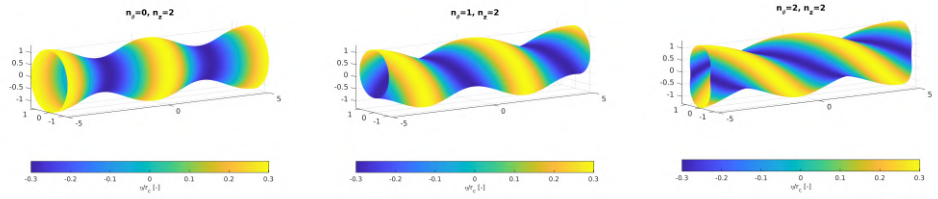

(g) Draft of the natural mode $n_z = 2, n_\theta = 0$ (h) Draft of the natural mode $n_z = 2, n_\theta = 1$ (i) Draft of the natural mode $n_z = 2, n_\theta = 2$

Figure 5.3: Drafts of some natural modes for the three-dimensional vortex cavitation.

where the terms with subscript $_c$ are relative to the cavity, W_c is the axial velocity near the cavity interface, W_∞ is the axial velocity in the far-field, $\Omega = \frac{V_\theta(r_c)}{r_c}$ is the angular velocity in correspondence of the cavity; K_σ is a term that represents the stiffness of the problem and is defined as:

$$K_\sigma = \frac{(p_\infty - p_v)}{\frac{1}{2}\rho W_\infty^2} \frac{r_c^2}{r_c^2 + r_v^2} \tag{5.4}$$

The term T_ω represents the surface tension contribution and is evaluated through the equation

$$T_\omega = (k_z, n_\theta) = \sqrt{1 + \frac{1}{K_\sigma We} \left(n_\theta^2 + k_z^2 r_c^2 + 1\right)} \tag{5.5}$$

where $We = \frac{\rho W_\infty^2 r_c}{\sigma}$ is the Weber Number. $H_{n_\theta}^{(1)}$ and $H_{n_\theta}^{(1)'}$ are the Hankel function and its derivative respectively. The last term in equation (5.3) is the value of the radial wave length k_r that is related to the axial wavelength and n_θ through the relation:

$$k_r^2 = \frac{1}{c^2}\left(\omega - W k_z\right)^2 - k_z^2 \tag{5.6}$$

In our case, since we are considering an incompressible flow, the speed of sound $c \to \infty$ and the radial wave number reduces to:

$$k_r = i k_z \tag{5.7}$$

5.2.2 Numerical settings

The simulation of these natural modes is developed with a three-dimensional mesh characterized by different regions:

- core region, almost Cartesian;
- inner cavity region, to match the core region and the interface region, through a stretching of the cells in the radial direction with cells smaller on the outer part as shown in Figure 5.4;
- Interfacial region, an area with very small cells, without stretching and a perfectly axial-symmetrical mesh;
- external region, perfectly axial-symmetrical region with cells relaxed along the radial direction to allow setting the external boundary far enough from the vortex core.

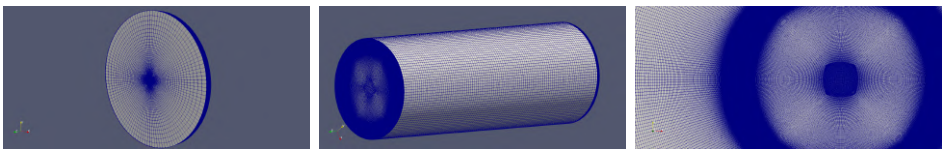

(a) external region (b) piece of mesh used for the vapor cavity (c) mesh detail 2

Figure 5.4: Pictures of the mesh used to simulate the 3D vortex with helicoidal perturbation.

The detail of the mesh used are collected in Table 5.2.

To correctly set the initial shape of the cavity, we set the vapor fraction α_l considering equation (5.2); in particular, we set:

$$\alpha_l = 0.01 \quad if \quad r\left(r, \theta, z\right) < r_c\left(\theta, z\right) \tag{5.8}$$

Characteristics	Value	
Max radius mesh	1	(m)
Radius external/interface region	0.02	(m)
Radius interface/inner cavity regions	0.015	(m)
Half core-region length	0.0025	(m)
Axial length	0.1	(m)

Table 5.2: Characteristics of the mesh used for the simulations.

where the local radius r_c is evaluated considering a perturbation equal to 0.02% of the analytical value of the equilibrium radius of the cavity: $\eta_0 := 0.02 * r_{c,0}$ and the natural mode associated to the pair $n_\theta = 2, n_z = 1$ was chosen for the simulations. The parameters of the simulations are summarized in Table 5.3

Characteristic	Symbol	Value	
Vortex circulation	Γ_∞	1	(m^2/s)
viscous radius	r_v	0.01	(m)
Reference pressure	p_{ref}	30000	(kg/ms^2)
Liquid density	ρ_l	1000	(kg/m^3)
Liquid viscosity	ν_l	0	(m^2/s)
Vapor density	ρ_v	0.02308	(kg/m^3)
Vapor viscosity	ν_v	0	(m^2/s)
Vapor pressure	p_v	2300	(Kg/ms^2)
Number of tangential perturbations	n_θ	2	
Number of axial perturbations	n_z	1	
Interface perturbation	$\frac{\eta_0}{r_c}$	0.02	
Bubble density	n	$1.6 * 10^{13}$	$(1/m^3)$
Nucleus radius	d_{Nuc}	$2 * 10^{-6}$	(m)
Condensation coefficient	C_c	1	
Vaporization coefficient	C_v	1	

Table 5.3: Fluid and field characteristic for the simulations with the helicoidal perturbation.

For this problem, three different values of axial velocity are considered, respectively $[1, 10, 200]\, m/s$; Figure 5.5 shows how the frequencies associated to homogeneous mode and the natural mode considered $(n_\theta = 2, n_z = 1)$ change as function of the axial velocity of the flow; in Figure 5.5 the three vertical dots lines represent the three axial velocities considered for the simulations.

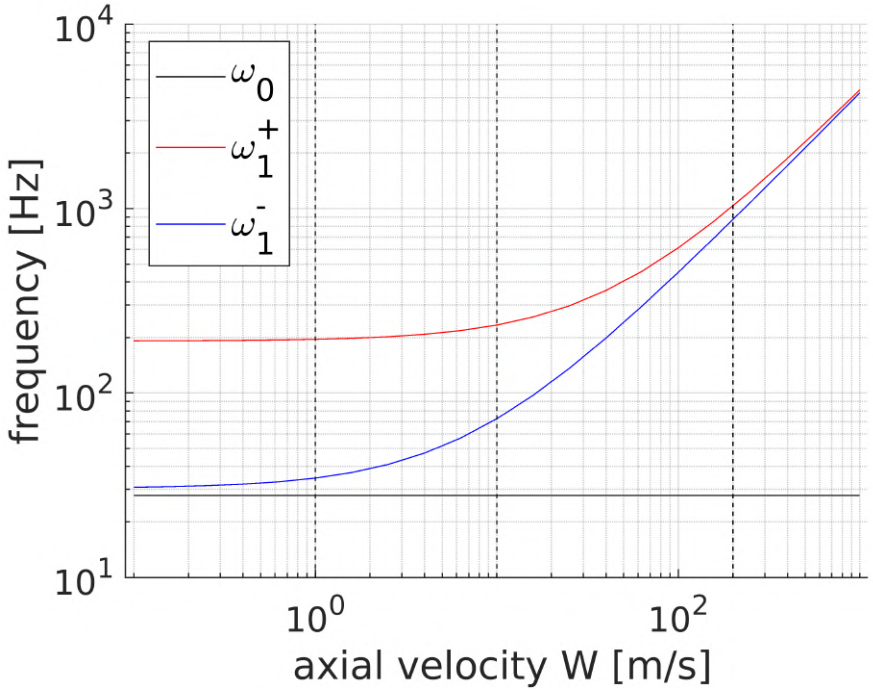

Figure 5.5: Analytical value of the frequencies as a function of the axial velocity for the natural mode $[n_z = 1, n_\theta = 2]$.

5.2.3 Axial velocity $W = 1m/s$

The first simulations carried out are those where the axial velocity was set equal to $W = 1m/s$. Note that in this case the pulsating frequency is close to the first rotational frequency. Two different simulations with this setting were carried out, one with mass transfer,(setting $C_c = C_v = 1$) and the other without mass transfer, thus setting the coefficients $C_c = C_v = 0$. These two simulations were run to identify the effect of the cavitation source terms on the dynamics of the vortex. Using the sets of probes as previously described and shown in Figure 5.2 the radius of the interface was evaluated at several axial-positions and at each time step $r_c(z,t)$. Specifically, at each time step we calculate the mean radius along the axial direction $\bar{r}_c(t)$, so that we can define the local perturbation as:

$$\eta(z,t) = r_c(z,t) - \bar{r}_c(t) \tag{5.9}$$

To study the dynamics of the vortex, both values of the radius of the cavity and the perturbation were analyzed through a Fourier analysis and the results were compared with the analytical values of the expected frequencies. The first simulation analyzed is that with an axial velocity equal to $W = 1\ m/s$ and with mass transfer. We report in Figure 5.6a the spectra of η

and r_c related to the different z-locations. Vertical dashed lines indicate the frequencies calculated analytically ω_0, ω_1^- and ω_1^+. Peak is visible in correspondence of the pulsating frequency ω_0 , which in this case is very close to the lower rotational frequency ω_1^-. Also, a small peak at the higher rotational frequency ω_1^+ is present. Noteworthy is the broadband profile in the low-frequency range, which is due to the effect of the homogeneous pulsation. Indeed, looking at the spectra of the perturbation η, Figure 5.6b, a clear tonal behavior is observed, for every location z.
Moreover, in this case all frequencies of the signal emerge more clearly, as well as some sub/super-harmonics. These harmonics may be due to the presence of higher/lower modes which are excited by the initial conditions.
The second simulation carried out is the one with the axial velocity $W =$

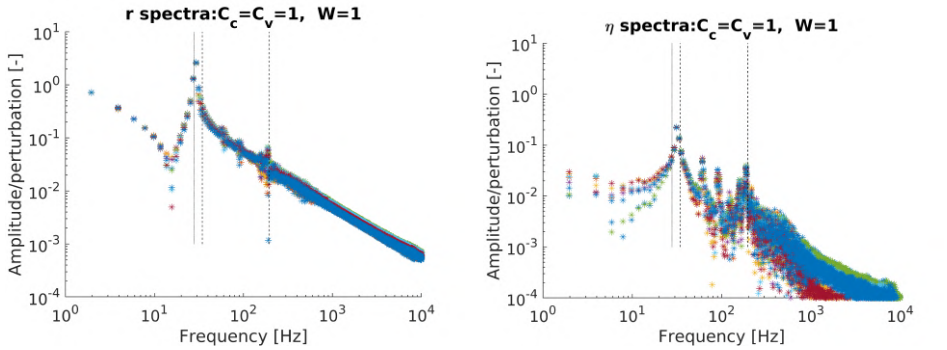

(a) Time spectra of the radius $r_c\,(z,t)$ evaluated for several axial position z.

(b) Time spectra of the perturbation η evaluated for several axial position z.

Figure 5.6: Spectra of the radius r and the perturbation η for the simulation with $C_c = C_v = 1$ and $W = 1\,m/s$.

$1m/s$ but without mass transfer, and this effect was imposed by setting to zero the coefficients controlling the mass transfer model $C_c = C_v = 0$: in this case, as visible in the plots 5.7a and 5.7b, the radius and the perturbation spectra have very well visible peaks on the frequencies related to the natural mode imposed as initial condition. There are no substantial differences between the two Figures, meaning that the cavity volume doesn't change in time and the frequency related to the homogeneous pulsating mode is not visible, in fact the homogeneous mode is related to the variation of the cavity volume.

5.2.4 Axial velocity $W = 10m/s$

Since in the first cases ($W = 1\,m/s$) the frequency of the homogeneous pulsating mode ω_0 is very close to the lower rotational frequency ω_1^-, two simulations with a different axial velocity were carried out. In fact, the

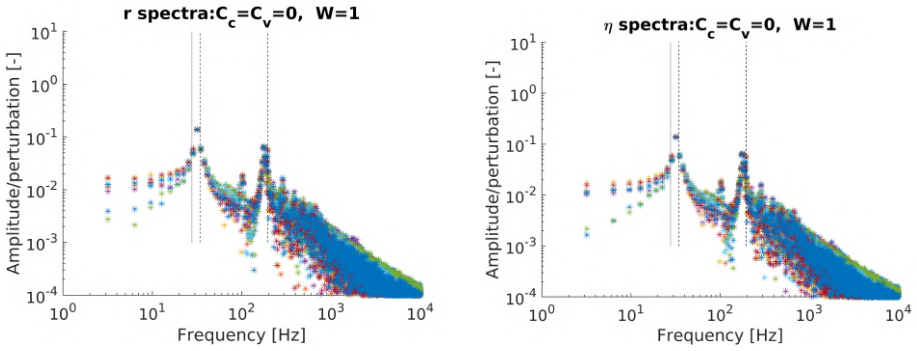

(a) Time spectra of the radius $r_c\,(z,t)$ evaluated for several axial position z.

(b) Time spectra of the perturbation η evaluated for several axial position z.

Figure 5.7: Spectra of the radius r and the perturbation η for the simulation with $C_c = C_v = 0$ and $W = 1\,m/s$.

variation of the axial velocity produces different values of $\omega_1^{\pm}$, as reported in the previous Figure 5.3.
The same analysis of the previous case is performed. Specifically, we evaluate the time-spectra of r_c and η, considering mass transfer ($C_c = C_v = 1$) in Figure 5.8 and deactivating it ($C_c = C_v = 0$), Figure 5.9.
The peaks related to the values of $\omega_1^{\pm}$ are well evident in all spectra. We notice that the increased axial velocity gives rise to a signal dominated by the rotation of the helical shape, in spite of a minor effect due to the pulsation. In case of mass transfer, and when considering the radius signal (Figure 5.8a) we still observe a broad-band behavior at very low frequencies. Some aspects still needs further investigations, such as the appearance of other harmonics when deactivating the mass transfer (Figure 5.9).

5.2.5 Axial velocity $W = 200m/s$

The third axial velocity tested is $W = 200m/s$. As the previous cases, we run the case with $C_v = C_c = 1$, as reported in the time-spectra of Figures 5.10; in these plots the modes related to the rotating helicoidal shape have the dominant and well visible peaks. Only in the radius spectra, depicted in Figure 5.10a, also an other high value appears, and it is the one related to the variation of the mean radius in time, in fact it isn't present in the plot for the perturbation, visible in Figure 5.10b.

The last simulation is the one with a high value of axial velocity $W = 200m/s$ but without mass transfer, $C_c = C_v = 0$. During this simulation the results for the radius and the perturbation are the same between each other, as depicted in Figure 5.11, and the spectra show very well defined and visible peaks for the helicoidal mode.

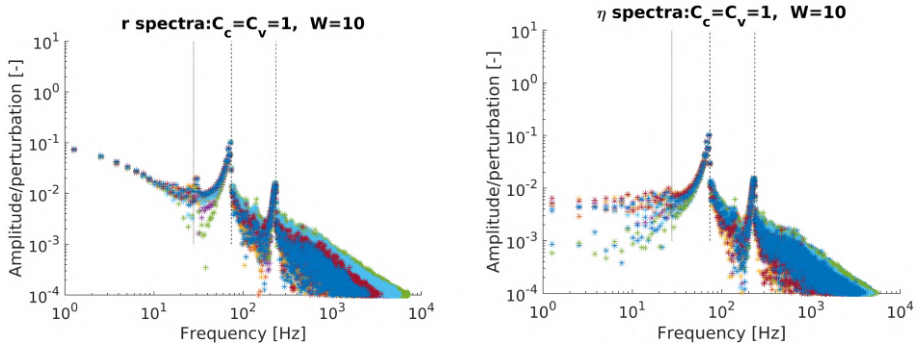

(a) Time spectra of the radius $r_c(z,t)$ evaluated for several axial position z.

(b) Time spectra of the perturbation η evaluated for several axial position z.

Figure 5.8: Spectra of the radius r and the perturbation η for the simulation with $C_c = C_v = 1$ and $W = 10\,m/s$.

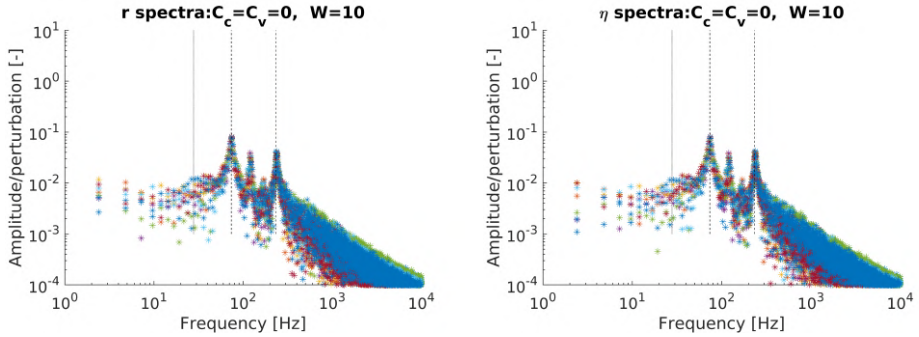

(a) Time spectra of the radius $r_c(z,t)$ evaluated for several axial position z.

(b) Time spectra of the perturbation η evaluated for several axial position z.

Figure 5.9: Spectra of the radius r and the perturbation η for the simulation with $C_c = C_v = 0$ and $W = 10\,m/s$.

To summarize, we can say that the dynamics of the cavitating vortex has been correctly reproduced. The natural modes associated to the pulsating oscillation and to the rotation of an helicoidal shaped cavity have been observed. Also, with higher values of the axial velocity we observed a dominant contribution from the rotational motion. Finally, the pulsating mode has been associated to the phase-change process, mostly visible in the low-axial-velocity case.

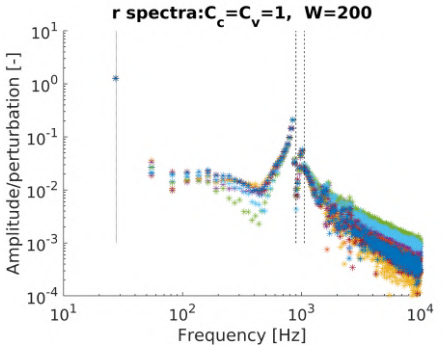

(a) Time spectra of the radius $r_c\,(z,t)$ evaluated for several axial position z.

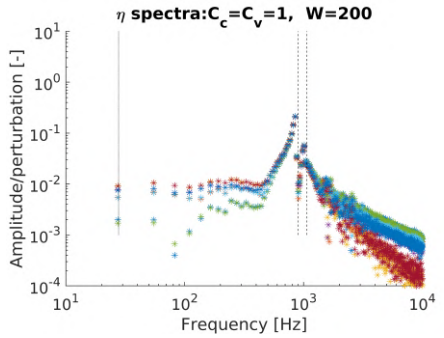

(b) Time spectra of the perturbation η evaluated for several axial position z.

Figure 5.10: Spectra of the radius r and the perturbation η for the simulation with $C_c = C_v = 1$ and $W = 200\,m/s$.

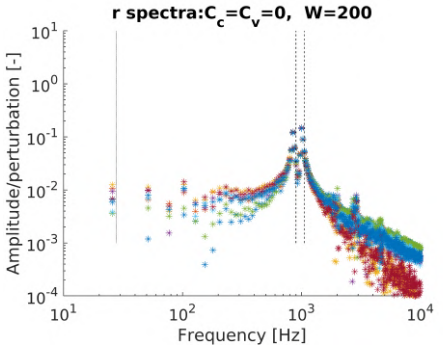

(a) Time spectra of the radius $r_c\,(z,t)$ evaluated for several axial position z.

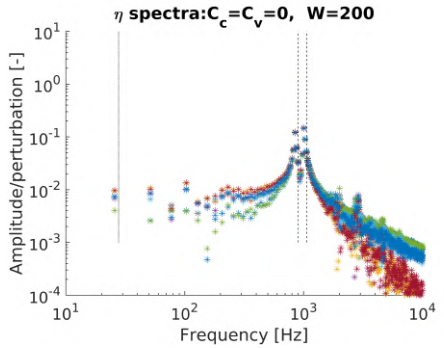

(b) Time spectra of the perturbation η evaluated for several axial position z.

Figure 5.11: Spectra of the radius r and the perturbation η for the simulation with $C_c = C_v = 0$ and $W = 200\,m/s$.

5.3 Concluding Remarks

In this Chapter, we reproduced numerically and analyzed the case of an idealized cavitating vortex, comparing the results with the analytical solution available in literature [Bosschers (2018)]. Different numerical and physical configurations were considered and analyzed, under the hypothesis of incompressible and inviscid flow. In particular, the study concerns the analysis of an isolated cavity forced to oscillate in an axial-homogeneous pulsating mode (analogous to the two-dimensional vortex case) or forced to oscillate with higher modes related to both axial and tangential wavenumbers; the study of the homogeneous pulsating mode was carried out by imposing a pressure jump at the boundary to force an initial non-equilibrium condi-

tion. It should be noted that the grid was built specifically to accurately capture the interface, optimized after several tests on different mesh types. When using coarse meshes, the cavity exhibited a damping of the mean radius in time; this behavior was observed also when increasing the parameters C_c and C_v of the cavitation model. Other tests were performed on the influence of these parameters, and numerical instability was experienced for high values of C_c and C_v.
A three-dimensional helicoidal natural mode of the isolated cavitating vortex was simulated with three different values for the axial velocity and considering the simulation with and without mass transfer between the two phases. Results showed a generally good agreement with the analytical solution, that we used to evaluate the characteristic frequencies of the motion. When considering a low axial velocity, the pulsating mode is dominant, in case the mass transfer is switched on. In this regard, we should note that the model presented by Bosschers does not account for mass transfer, but rather it includes cavity compressibility. Thus, the oscillating pattern we observe comes from different physical constraints. We believe that this point may deserve further study. For higher values of axial velocity and/or in general switching the mass transfer model off, the rotational frequencies related to the helicoidal shape are well represented. In all cases herein investigated, we observed that volume oscillation of the cavity related to the pulsating mode is an important process that can be accurately reproduced using the mixture model even under the assumption of incompressible flow.

Conclusions

This thesis was devoted to the analysis of different aspects of the cavitation modelling. SInce the dynamics of the cavitation is strictly related to the dynamics of vapor bubbles dispersed in water, we started the analysis investigating the stability of a bubble using the equation of Rayleigh-Plesset [Plesset and Prosperetti (1977)], Specifically, we analized the stability conditions and the equilibrium of the bubble with a parametric study considering the values of the pressure of the non-condensable gas and the external liquid pressure. This study can be useful to improve standard cavitation models, as, for example, the Schnerr-Sauer model [Schnerr and Sauer (2001)] that considers the bubbles under the hypothesis of asymptotic growth. Then we analyzed four different cavitation models, available in literature, which rule the phase-change within the mass transfer approach. The analysis was performed considering the case of a two-dimensional laminar flow around a cylinder. The results obtained in this study clearly showed that the cavity dynamics may largely vary depending on the specific model considered. In particular, the choice of the model influences the amount of vapor obtained in the simulation as well as the cavitation regime predicted. This may depend on the empirical and, somewhat arbitrary choice of the constants. To overcome this problem we developed an analytical, physical-based method to normalize the coefficients of vaporization and condensation, forcing them to develop or slump a specific amount of vapor over a characteristic time scale of the process, considering an archetypal situation for the transport equation.
The four models were tested using, first, the standard coefficients and , successively, using the normalized coefficients. We found that the the use of the normalized coefficients made the models to behave in a more physical way, predicting better the cavitation regime and the amount of vapour released. In the last part of this thesis we performed a numerical study to analyze the dynamics of a cavitating vortex. The importance of this part relies on the practical importance of the freely evolving vortices in hydrodynamic applications. In fact, the idealized vortex can be a convenient representation of the tip vortex which forms downstream a ship propellers, and its study may be important for the noise emission problems associated to cavitating propellers. Two and three dimensional vortex structures were considered. We

simulated and analyzed the oscillatory dynamics of the vortex with a pulsating mode, comparing the results with the analytic results found in literature [Bosschers (2018)] and valuating the effect of the numerical configuration in terms of the mesh characteristics and refinement, coefficients for the cavitation model and time step; The study pointed out that the coefficients do not influence the dynamics of the vortex. An important conclusion highlighted by these results can be that the variation of the coefficients is very important in the case of cloud or sheet cavitation and less relevant in the case of flow-driven cavitation. However, high values for the condensation/vaporization coefficients led to numerical damping and instability. Also the mesh was found to be very important in this kind of simulations; a too coarse mesh induced damping of the cavity radius, while a too fine mesh led to numerical instability. Also, the use of typical cartesian shaped grids in the region of the interface may lead to spurious interfacial velocities. The optimal grid shape is axial symmetric in the region of interface between the cavity and the liquid phase. As final step a helicoidal natural mode of the three-dimensional cavitating vortex was simulated considering three different axial velocities and considering the cases with and without mass transfer: during these simulation we noted that the forced mode was found always visible. We also noted that, when the mass transfer model is active, the pulsating mode may be dominant for the low axial velocity cases. The results of this study may be applied to the analysis of tip vortex cavitation often present in the wake of ship propellers.

Bibliography

[Bosschers (2018)] Bosschers J. Propeller Tip-vortex cavitation and its brandband noise, Ph.D. thesis **2018**.

[Brackbill et al. (1992)] Brackbill J. U., Kothe D. B., Zemach C. A continuum method for modeling surface tension. *Journal of computational physics*, **1992**, *100.2*, 335–354.

[Brennen (1995)] Brennen, C. Cavitation and Bubble Dynamics *Oxford University Press: Oxford, UK*, **1995**.

[Burnham and Hallock (1982)] Burnham D. C., Hallock J.N. Chicago Monostatic Acoustic Vortex Sensing System. Volume IV. Wake Vortex Decay. TRANSPORTATION SYSTEMS CENTER CAMBRIDGE MA, **1982**.

[Coutier-Delgosha et al. (2005)] Coutier-Delgosha O., Fortes-Patella R., Reboud J.L., Hakimi N., Hirsch C. Stability of preconditioned Navier–Stokes equations associated with a cavitation model. *Comput. Fluids*, **2005**, *34*, 319–349.

[Delannoy and Kueny (1990)] Delannoy, Y.; Kueny, J.L. Two phase flow approach in unsteady cavitation modeling. *ASME Cavitation Multiph. Flow Forum*, **1990**, *109*, 153–159.

[Franc (2006)] Franc J. P., Physics and Control of Cavitation, University of Grenoble, France, RTO-EN-AVT-143, **2006**.

[Fry (1984)] Fry, S. Investigating cavity/wake dynamics for a circular cylinder by measuring noise spectra. *J. Fluid Mech.*, **1984**, *142*, 187–200.

[Gaggero and Villa (2017)] Gaggero, S.; Villa, D. Steady cavitating propeller performance by using OpenFOAM, StarCCM+ and a boundary element method. *Proc. Inst. Mech. Eng. Part M J. Eng. Marit. Environ.*, **2017**, *231*, 411–440.

[Garamani et al. (2021)] Ghahramani, E.; Ström, H.; Bensow, R. Numerical simulation and analysis of multi-scale cavitating flows. *J. Fluid Mech.*, **2021**, *922*.

[Ghahramani et al. (2007)] Ghahramani E.,Arabnejad Khanouki M., Bensow R., A Hybrid Model for Simulation of cavitating flows;*12th OpenFOAM workshop*, **2007**

[Gnanaskandan and Mahesh (2016)] Gnanaskandan, A.; Mahesh, K. Numerical investigation of near-wake characteristics of cavitating flow over a circular cylinder. *Int. J. Fluid Mechanics*, **2016**, *790*, 453–491.

[Jacqmin (1999)] Jacqmin, D. Calculation of two-phase Navier–Stokes flows using phase-field modeling. *Journal of computational physics*,**1999**, *155.1*, 96–127.

[Joukowsky (1900)] Joukowsky, N. UBer den Hydraulischen Stoss in Wasserleitungsrohren, Acadmie Impriale Des Sciences, St. Petersburg, Russia,**1900**.

[Kornfeld and Suvorov (1944)] Kornfeld, M., and L. Suvorov. On the destructive action of cavitation.*Journal of Applied Physics*, **1944**, *15.6*, 495–506.

[Kubota et all. (1992)] Kubota A., Kato H., Yamaguchi H. A new modeling of cavitating flows: a numerical study of unsteady cavitation on a hydrofoil section *J. Fluid Mech.*, **1992**, *240*, 59–96.

[Kunz et al. (2000)] Kunz R.F., Boger D.A., Stinebring D.R., Chyczewski T.S., Lindau J.W., Gibeling H.J., Venkateswaran S., Govindan T.R. A preconditioned Navier–Stokes method for two-phase flows with application to cavitation prediction. *Comput. Fluids*, **2000**, *29*, 849–875.

[Lu (2008)] Lu, N. Available online: `http://www.tfd.chalmers.se/~hani/kurser/OS_CFD_2008/NaixianLu/REPORT_interPhaseChangeFoam.pdf` (accessed on June 2020).

[Matsudaira et al. (1992)] Matsudaira, Y.; Gomi, Y.; Oba, R. Characteristics of bubble-collapse pressures in a Karman-vortex cavity. *JSME Int. J.*, **1992**, *35*, 179–185.

[Merkle et al. (1998)] Merkle C.L., Feng J., Buelow P.E.O. Computational modelling of the dynamics of sheet cavitation. *Proceedings of the 3rd International Symposium on Cavitation, Grenoble, France*, **1998**.

[Morgut and Nobile (2012)] Morgut, M.; Nobile, E. Numerical Predictions of Cavitating Flow around Model Scale Propellers by CFD and Advanced Model Calibration. *Int. J. Rotating Mach.* **2012**, 618180.

[Plesset (1949)] Plesset M. S. The dynamics of cavitation bubbles. **1949**.

[Plesset and Prosperetti (1977)] Plesset M. Prosperetti A. Bubble Dynamic and Cavitation. *Ann. Rev. Fluid Mech.* **1977**, *9*, 145–185.

[Plesset and Zwick (1952)] Plesset M., Zwick A. The growth of vapor bubbles in superheated liquids.*Journal of applied physics*, **1954**, *25.4*, 493–500.

[Prosperetti and Lezzi (1986)] Prosperetti A., Lezzi A. Bubble dynamics in a compressible liquid. Part 1. First-order theory. *Journal of Fluid Mechanics* **1986**,*168*, 457–478.

[Qin et al. (2003)] Qin Q., Song C.C.S., Arndt R.E.A. A virtual single-phase natural cavitation model and its application to Cav2003 hydrofoil. *Proceedings of the 5th International Symposium on Cavitation, Osaka , Japan*, **2003**.

[Rayleigh (1917)] Rayleigh L. On the pressure developed in a liquid during the collapse of a spherical cavity. *The London, Edinburgh, and Dublin Philosophical Magazine and Journal of Science*,**1917**, *34.200*, 94–98.

[Rebound et al. (1998)] Reboud J.L., Stutz B., Coutier-Delgosha O. Two phase flow structure of cavitation: experiment and modeling of unsteady effects.*Proceedings of the 3rd International Symposium on Cavitation, Grenoble, France*, **1998**.

[Roohi et al. (2013)] Roohi E., Zahiri A.P., Passandideh-Fard M. Numerical simulation of cavitation around a two-dimensional hydrofoil using VOF method and LES turbulence model. *Appl. Math. Model.* **2013**, *37*, 6469–6488.

[Saito et al. (2007)] Saito Y., Takami R., Nakamori I., Ikohagi T. Numerical analysis of unsteady behavior of cloud cavitation around a NACA0015 foil. *Comput. Mech.* **2007**, *40*, 85–96.

[Schnerr and Sauer (2001)] Schnerr G.H., Sauer J. Physical and Numerical Modeling of Unsteady Cavitation Dynamics. *Proceedings of the 4th International Conference on Multiphase Flow, New Orleans, LA, USA* **2001**.

[Senocak and Shyy (2004)] Senocak I., Shyy W. Interfacial dynamics-based modelling of turbulent cavitating flows, Part-1: Model development and steady-state computations *Int. J. Numer. Meth. Fluids*, **2004** *44.9* 975–995.

[Singhal et al. (1997)] Singhal A.K., Vaidya, N., Leonard A.D. Multi-dimensional simulation of cavitating flows using a PDF model for phase change. *Proceedings of the ASME Fluids Engineering Division Summer Meeting, Vancouver, BC, Canada*, **1997**.

[Song and He (1998)] Song C., He G. Numerical simulation of cavitating flow by single-phase flow approach. *Proceedings of the 3rd International Symposium on Cavitation, Grenoble, France*, **1998**.

[Sun et al. (2012)] Sun D., Xu J., Wang L. Development of a vapor–liquid phase change model for volume-of-fluid method in FLUENT, *International Communications in Heat and Mass Transfer*, **2012**, *39.8*, 1101–1106.

[Sussman et al. (1994)] Sussman M., Smereka P., Osher S. A level set approach for computing solutions to incompressible two-phase flow. *Journal of Computational physics,114(1)* **1994**, 146–159.

[Unverdi and Tryggvason (1992)] Unverdi S. O., Tryggvason G. A front-tracking method for viscous, incompressible, multi-fluid flows. *Journal of computational physics*, *100.1* **1992**, 25–37.

[Yang and Mao (2005)] Yang C., Mao Z. Numerical simulation of interphase mass transfer with the level set approach. *Chemical Engineering Science 60.10* **2005**, 2643–2660.

[Zhou et al. (2019)] Zhou H., Xiang M., Okolo P., Wu Z., Bennett G., Weihua Z. An efficient calibration approach for cavitation model constants based on OpenFOAM platform. *J. Mar. Sci. Technol.* **2019**, *24*, 1043–1056.

[Zwart et al. (2004)] Zwart P.J., Gerber A.G., Belamri T. A two-phase flow model for predicting cavitation dynamics. *Proceedings of the International Conference on Multiphase Flow, Yokohama, Japan*, **2004**.

[www.vesselfinder.com] `https://www.vesselfinder.com/news/21134-First-DNV-SILENT-E-class-notation-awarded-to-a-merchant-vessel`(accessed on November 2022)

Acknowledgements

First of all, I would like to thank Professor Armenio for allowing me to follow this path and for guiding me throughout the period, Dott. Cianferra whose help was fundamental to me during my journey, and Professor Bensow who allowed me to have a fantastic experience in Göteborg. All the friends, now close or far away, who comforted me in my darkest moments and who undeterred listened to me talk about the doubts that afflicted me despite not following my twisted reasoning. But above all, I have to thank all my family for the constant support they have always given me and for continuing to believe in me, even when I doubted myself.

Trieste, 28.09.2023

Andrea Savio